

SDSS-IV MaNGA: Bayesian analysis of the star formation history of low-mass galaxies in the local Universe

Shuang Zhou^{1*}, H.J. Mo^{2,1}, Cheng Li¹, Médéric Boquien³, Graziano Rossi⁴

¹*Department of Astronomy, Tsinghua University, Beijing 100084, China*

²*Department of Astronomy, University of Massachusetts Amherst, MA 01003, USA*

³*Centro de Astronomía, Universidad de Antofagasta, Avenida Angamos 601, Antofagasta 1270300, Chile*

⁴*Department of Astronomy and Space Science, Sejong University, 209, Neungdong-ro, Gwangjin-gu, Seoul, South Korea*

Last updated 2015 May 22; in original form 2013 September 5

ABSTRACT

We measure the star formation histories (SFH) of a sample of low-mass galaxies with $M_* < 10^9 M_\odot$ from the SDSS-IV MaNGA survey. The large number of IFU spectra for each galaxy are either combined to reach a high signal to noise ratio or used to investigate spatial variations. We use Bayesian inferences based on full spectrum fitting. Our analysis based on Bayesian evidence ratio indicates a strong preference for a model that allows the presence of an old stellar population, and that an improper model for the SFH can significantly underestimate the old population in these galaxies. The addition of NIR photometry to the constraining data can further distinguish between different SFH model families and significantly tighten the constraints on the mass fraction in the old population. On average more than half of the stellar mass in present-day low-mass galaxies formed 8 Gyrs ago, while about 30% within the past 4 Gyrs. Satellite galaxies on average have formed their stellar mass earlier than central galaxies, and stars in the outer regions of galaxy are younger than those in the central part. Our results suggest that most of the low-mass galaxies have an early episode of active star formation that produces a large fraction of their present stellar mass.

Key words: galaxies: fundamental parameters – galaxies: stellar content – galaxies: formation – galaxies: evolution

1 INTRODUCTION

Star formation in galaxies is regulated by a wealth of complex physical mechanisms, such as the formation, growth and merger of dark matter halos, and the cooling and heating of baryon gas by radiative and feedback processes. Characterising the star formation history of observed galaxies represents, therefore, an important step in understanding how galaxies form and evolve. Despite being the most abundant type of galaxy in the universe, dwarf (low-mass) galaxies remain elusive as far as their formation and evolution is concerned. Their observed blue colour is usually taken as an indication that these galaxies are dominated by young stellar populations (e.g. Kauffmann et al. 2003). By studying stacked spectra from the Sloan Digital Sky Survey (SDSS), Heavens et al. (2004) found a very different formation history between low- and high-mass galaxies. While galaxies with stellar masses smaller than $10^{10} M_\odot$ could be well represented by a flat star formation rate over the past 3 Gyr and a declining rate towards earlier epochs, more massive galaxies generally form most of their stellar masses earlier. Recent investigations about low-mass galaxies, however, challenge the stereotype that low-mass galaxies are all young. For local group dwarf galax-

ies in which individual stars can be resolved, the star formation history can be obtained through ‘archaeological’ age reconstruction (e.g. Mateo 1998; Dolphin et al. 2005; Aloisi et al. 2007; Tolstoy et al. 2009; Weisz et al. 2011; Annibali et al. 2013; Weisz et al. 2014; Sacchi et al. 2016; Albers et al. 2019). The analysis based on the colour-magnitude diagram of resolved stellar populations in general suggests that most stars in dwarf galaxies were formed more than 5 Gyr ago. For example, Weisz et al. (2011) analysed the star formation histories (SFHs) of 60 nearby ($D < 4$ Mpc) dwarf galaxies and found that these galaxies on average have formed half of their stars before $z \sim 2$, regardless of their morphological types. The existence of such an old stellar population is supported by other types of observations. Using the CANDELS survey, van der Wel et al. (2011) found a population of extreme emission line galaxies at redshift $z \sim 1.7$, with a number density so high that they can contribute a significant fraction of the total stellar mass contained in present-day dwarf galaxies with masses between 10^8 and $10^9 M_\odot$. These authors suggested that most of the stellar mass of these dwarf galaxies should have formed before $z \sim 1$. Kauffmann (2014) used the 4000 Å break and $H\delta_A$ indices in combination with SFR/M_* derived from emission line measurements to constrain the SFHs of a sample of SDSS galaxies with stellar masses in the range $10^8 - 10^{10} M_\odot$, and concluded that galaxies with stellar masses

* Contact e-mail: szhou@mail.tsinghua.edu.cn

smaller than $10^9 M_\odot$ are not all young but with half-mass formation times ranging from 1 to 10 Gyr. Similar conclusions have also been reached by spectral energy distribution (SED) modelling of a sample of blue compact dwarf galaxies with masses between 10^7 and $10^9 M_\odot$ (Janowiecki et al. 2017) and a sample of HII galaxies (Telles & Melnick 2018). Stars in most of these galaxies are best described by two or more stellar populations, with the oldest population often dominating the stellar mass.

In agreement with those observations, the empirical model presented in Lu et al. (2014) and Lu et al. (2015) predicts that dwarf galaxies in small dark matter halos ($M_h < 10^{11} h^{-1} M_\odot$) had a strong episode of star formation at $z > 2$, producing significant amounts of old stars in them. However, such an old population is not predicted in many other models (Lim et al. 2017). SFHs of low-mass galaxies have also been investigated using hydrodynamical simulations. For example, Digby et al. (2019) analyzed the SFHs of a number of field and satellite dwarf galaxies in the APOSTLE and Auriga simulations, and found that the predicted star mass fractions of stars of different ages are quite different from those observed in real surveys. Garrison-Kimmel et al. (2019) analyzed about 500 dwarf galaxies in the FIRE-2 zoom-in simulations and found that the cumulative SFHs of the simulated galaxies do not match those observed.

Clearly, accurate measurements of SFHs of low-mass galaxies can provide important constraints on galaxy formation models. However, the investigations so far have their limitations. For example, the number of dwarf galaxies for which stars can be resolved is very limited (Weisz et al. 2011), and so it is difficult to draw reliable statistical conclusions. Methods based on SED fitting (e.g. Janowiecki et al. 2017; Telles & Melnick 2018) can make use of galaxy photometry over a wide wavelength coverage, but they may lose spectral features that contain information about the SFH. This shortcoming may be remedied by methods using galaxy spectra, but high SNR spectra are needed to probe the faint old stellar population. The stacking of spectra of individual galaxies has been used to achieve a high enough SNR for such analysis (e.g. Kauffmann 2014), but such stacking mixes the signals of individual galaxies.

Here we intend to make our contribution by analyzing a sample of low-mass galaxies selected from the Mapping Nearby Galaxies at Apache Point Observatory (MaNGA; Bundy et al. 2015). With its integral-field spectroscopy (IFS), MaNGA provides a large number of integral-field unit (IFU) spectra of individual galaxies. These not only allow us to obtain high signal-to-noise composite spectra for individual galaxies, which is essential for constraining the SFH in detail, but also to study spatial variations of the SFH within individual galaxies. The large sample of low-mass galaxies also makes it possible to study how the SFH depends on other galaxy properties. In addition, MaNGA is designed to overlap as much as possible with other observations, which allows us to make use of information from other observations, thereby to get more observational constraints. Our analysis is based on our newly developed stellar population synthesis (SPS) code, Bayesian Inference for Galaxy Spectra (BIGS), which has been successfully used to constrain the IMF of MaNGA early-type galaxies (Zhou et al. 2019). BIGS fits the full composite spectrum of a galaxy and constrains its SFH along with other properties of its stellar population. The Bayesian approach provides a statistically rigorous way to explore potential degeneracies in model parameters, and to distinguish between different models through Bayesian evidence. Moreover, the flexibility of BIGS also allows us to add new observational constraints in our inferences.

The paper is organised as follows. In §2 we present our data

reduction process, including sample selection and spectral stacking procedure. We then introduce the SPS model and the Bayesian approach used to fit galaxy spectra in §3. Our main results are presented in §4, and we discuss some potential uncertainties in §5. Finally, we summarize and discuss our results in §6. Throughout this work we use a standard Λ CDM cosmology with $\Omega_\Lambda = 0.7$, $\Omega_M = 0.3$ and $H_0 = 70 \text{ km s}^{-1} \text{ Mpc}^{-1}$.

2 DATA

2.1 The MaNGA survey

As one of the three core programmes in the fourth-generation Sloan Digital Sky Survey (SDSS-IV, Blanton et al. 2017), MaNGA aims to collect high resolution, spatially resolved spectra for about 10,000 nearby galaxies so as to infer the internal kinematic structure and composition of gas and stars in them. MaNGA targets are selected from the NASA Sloan Atlas catalogue¹ (NSA, Blanton et al. 2005) to cover the stellar mass range $5 \times 10^8 M_\odot h^{-2} \leq M_* \leq 3 \times 10^{11} M_\odot h^{-2}$, with median redshift $z \sim 0.03$. The MaNGA sample is selected so that the number density of galaxies is roughly independent of the i -band absolute magnitude, M_i (Wake et al. 2017). It consists of three sub-samples: the Primary, Secondary and Colour-Enhanced samples. For galaxies in the Primary and Secondary samples, the IFUs cover a radius up to $1.5R_e$ and $2.5R_e$ (R_e being the effective radius), respectively, while the Colour-Enhanced sample selects galaxies in regions that are not well sampled by the Primary sample in the NUV- i colour versus M_i plane. The sizes of the MaNGA IFUs vary for different galaxies, with a diameter ranging from $12''$ for a 19-fiber IFU to $32''$ for a 127-fiber IFU (Drory et al. 2015; Law et al. 2015).

MaNGA observes the selected galaxies with the two dual-channel BOSS spectrographs (Smee et al. 2013) on the Sloan 2.5 m telescope (Gunn et al. 2006), which provides simultaneous wavelength coverage over $3600 - 10,300 \text{ \AA}$, with a spectral resolution $R \sim 2000$ (Drory et al. 2015). The typical r -band signal-to-noise ratio (SNR) in the outskirts of MaNGA galaxies is 4 to 8 (\AA^{-1} per $2''$ fiber) at 23 AB mag arcsec⁻². The spectrophotometry calibration of MaNGA is described in detail in Yan et al. (2016a), while the initial performance is given in Yan et al. (2016b).

The observed IFU spectra are reduced by the MaNGA data reduction pipeline (DRP, Law et al. 2016). DRP produces sky-subtracted, spectrophotometrically calibrated spectra, and combines individually dithered observations into three dimensional data cubes of $\text{\AA} \times \text{spaxels} \times \text{\AA}$ with an angular size of $0.5'' \times 0.5''$. The relative flux calibration is better than 5% (Yan et al. 2016b). In addition, MaNGA provides measurements of stellar kinematics (velocity and velocity dispersion), emission-line properties (kinematics, fluxes, and equivalent widths), and spectral indices for each spaxel through the MaNGA Data Analysis Pipeline (DAP; Westfall et al. 2019), which uses the pPXF (Cappellari 2017) full spectral fitting technique to fit the stellar continuum and nebular emission lines of each spectrum.

2.2 UKIDSS

Near-infrared (NIR) photometric data are commonly used to trace the stellar mass of galaxies, which can be compared with the mass estimated from the stellar population synthesis modeling of the

¹ <http://www.nsatlas.org/>

optical spectra provided by MaNGA. As described in Yan et al. (2016a), the MaNGA targets are chosen to overlap as much as possible with the United Kingdom Infrared Telescope (UKIRT) Infrared Deep Sky Survey (UKIDSS) footprint. UKIDSS uses the Wide Field Camera (WFCAM) on the 3.8 m United Kingdom Infrared Telescope (UKIRT), providing ZYJHK images over a large sky coverage. The basic information of the survey can be found in Lawrence et al. (2007), and the photometric system is described in Hewett et al. (2006). The UKIDSS data is reduced by the official pipeline and the science products are released through the WFCAM Science Archive² (hereafter WSA, Hambly et al. 2008).

2.3 Sample selection

The galaxy sample used here is selected from the internal data release of MaNGA, the MaNGA Product Launch 7 (MPL-7), which includes a total of 4,621 unique galaxies and has been made public available together with the SDSS fifteen data release (SDSS DR15 Aguado et al. 2019). We select a set of the least massive galaxies ($M_* < 10^9 M_\odot$) according to their total stellar masses given by NSA. These total stellar masses are derived from the fit to the SDSS five-band photometry with K-corrections (Blanton & Roweis 2007), using the Bruzual & Charlot (2003) stellar population model and the Chabrier (2003) IMF. After excluding galaxies with apparent problems in data reduction and/or spectral fitting, we obtain a sample of 254 low-mass galaxies.

We then cross-match galaxies in this sample with data from WSA, selecting galaxies that have measurements of SDSS u , g , r , i , z and UKIDSS Y , J , H , K band magnitudes. This cross-match yields a total of 752 galaxies in MaNGA MPL7 and 22 of them are in the least massive sample. Considering potential differences between SDSS and MaNGA, such as flux calibrations, we convolve the spectrum of a galaxy obtained by stacking its spaxels within $1 R_e$ (see below) with the SDSS filters to derived its MaNGA ($g-r$) colour. We only select galaxies whose MaNGA ($g-r$) colours are within 0.05 mag of the ($g-r$) colours listed in WSA. This yields a final sample of 19 low-mass galaxies with both optical and NIR photometry.

In what follows, we use the sample of 254 low-mass galaxies selected from MaNGA to investigate the statistical properties of the SFHs of these galaxies, and use the 19 low-mass galaxies with photometry from UKIDSS to study additional constraints on the SFHs from the NIR photometry.

2.4 Spectral stacking

The original spectra provided by MaNGA DRP have typical r -band SNRs of $4-8 \text{ \AA}^{-1}$ in the outer parts of galaxies (Law et al. 2016). For the low-mass galaxies considered here, the SNR can be as low as 2 \AA^{-1} due to their relatively low surface brightness. One thus needs to combine spectra in each IFU plate of each individual galaxy to obtain a stacked spectrum with a sufficiently high SNR.

We use two kinds of stacked spectra of every individual galaxy. First, to study the global SFHs of individual galaxies and the overall variations of SFH from galaxy to galaxy, we co-add all the spaxels inside one effective radius (R_e , from NSA) of a galaxy to form a single spectrum. Second, to study the variations of the SFH within a galaxy, we divide spaxels of the galaxy into three radial bins, $(0.0-0.3)R_e$, $(0.3-0.7)R_e$ and $(0.7-1.2)R_e$, according

to their normalised radii of elliptical annuli given in MaNGA DAP, and stack the spectra within individual radial bins. These radial bins are similar to those used in related MaNGA studies, such as Zheng et al. (2019).

The binning procedure is as follows. To begin with, we use masks provided by the MaNGA DRP and DAP, collecting all quantities that are deemed problematic, such as low or no fibre coverage, and foreground star contamination. These masked individual pixels in the spectra from DRP, and the corresponding outputs of stellar velocity, v , and velocity dispersion, σ_* , from DAP are excluded. We then use the redshift z of each galaxy provided by NSA and stellar velocity v of each spixel extracted from MaNGA DAP to convert the wavelengths of each spectrum to the rest-frame. In the conversion, we use a cut at $\text{SNR} = 5$ to ensure the accuracy in the measurements of the kinematics. The flux, inverse-variance and spectral resolution vectors from DRP datacubes are interpolated to a common wavelength grid which is uniform in logarithmic space. A light-weighted average flux of each bin can then be obtained from the mean of the flux at each spixel within the corresponding bin.

Traditionally, the variance vectors of the stack spectra can be generated as the quadratic sum of the error vectors of individual spectra according to the noise propagation formula. In that case, the stacking of N individual spectra leads to an increase of the SNR by a factor of $N^{1/2}$, with N being the number of spaxels. For the stacking of MaNGA spectra here, however, the SNR of stack spectra deviates from the simple noise propagating formula, because the spaxels provided by DRP are not fully independent (see Westfall et al. 2019, for details). Here we use the correction term given by Westfall et al. (2019) to account for the covariance between spaxels and to estimate the SNR. The correction term can be written as

$$n_{\text{real}}/n_{\text{nocovar}} = 1 + 1.62 \log(N_{\text{bin}}) \quad (1)$$

where N_{bin} is the number of spectra used in the stacking, n_{real} and n_{nocovar} are the corrected noise vectors and noise vectors that assuming no covariance between pixels (namely, those generated from the simple noise propagating formula) respectively. With this correction, the typical SNR of the stacked spectra is around 40 pixel^{-1} . The SNR peaks at $\sim 6000 \text{ \AA}$ and drops towards both the red and blue ends.

3 ANALYSIS

To infer the SFHs from galaxy spectra, one needs to compare stellar population models with the observed spectra. This can be done either by using some absorption features that are sensitive to the SFH, such as Dn4000 and H_{δ_A} , or by fitting an entire spectrum with a combination of stellar population model spectra. These two approaches are complementary. The full spectrum in principle contains more information, but may suffer from strong degeneracy between different factors that can affect the spectrum of a galaxy. In contrast, selected absorption features may be sensitive to specific stellar populations, avoiding some degeneracy, but they may miss important information contained in the rest of the spectrum. In this paper, we adopt the full spectrum fitting method using Bayesian statistics to infer the SFH of a given individual galaxy and its covariance with other properties.

3.1 The spectral synthesis model

To accurately model galaxy spectra, proper templates that meet the resolution and wavelength coverage of the data are crucial. Sev-

² <http://wsa.roe.ac.uk/>

eral popular codes are available to model simple stellar populations (SSPs) of given ages and metallicity, including BC03 (Bruzual & Charlot 2003), M05 (Maraston 2005), Cvd12 (Conroy & van Dokkum 2012) and E-MILES (Vazdekis et al. 2016). These SSP models can be combined with an assumption of the SFH of a galaxy to predict its spectrum. Different SSP models are based on different stellar templates and isochrones, and thus have their own merits and shortcomings. Given that the wavelength range of the original MaNGA data is 3600 – 10300 Å, and the median redshift of MaNGA galaxies is $z \sim 0.03$, we select models that have uniform wavelength coverage to ~ 9000 Å. In addition, the UKIDSS data require an extension of the coverage to $\sim 2.5 \mu\text{m}$. With these considerations, we decide to adopt the E-MILES³ model.

The E-MILES model is the latest version of the MILES model originally presented in Vazdekis et al. (2010). It is constructed using the MILES (Sánchez-Blázquez et al. 2006), CaT (Cenarro et al. 2001) and Indo-U.S. (Valdes et al. 2004) empirical stellar libraries, and extended to the infrared using the IRTF stellar library (Cushing et al. 2005; Rayner et al. 2009). With all these stellar templates combined, the E-MILES SSP spectra cover the wavelength range from 1680.2 Å to 5 μm with a moderately high spectral resolution. In particular, the SSPs can reach a resolution of 2.51 Å (FWHM) over the range from 3540 Å to 8950 Å, which covers the main portion of the spectral range of MaNGA. The spectral resolution decreases towards longer wavelengths, but is sufficient for photometry calculations.

The E-MILES model is computed for several IMFs. As our focus is on low-mass galaxies, which tend to have a bottom-light IMF (Li et al. 2018), we choose the model constructed with the Chabrier IMF. Moreover, E-MILES provides two sets of isochrones, the Padova+00 isochrones (Girardi et al. 2000) and the BaSTI isochrones⁴. The impact of using different isochrones has not been investigated extensively in the literature. For MaNGA galaxies, Ge et al. (2019) found that using different isochrones does not lead to significant changes in the fitting quality of observed spectra. Using mock spectra, however, the authors found that the Padova+00 model works better at low metallicity ($[Z/H] < -1.0$), while the BaSTI model works better for galaxies of higher metallicity. Since low-mass galaxies in general are metal poor, we use E-MILES templates with Padova+00 isochrones.

3.1.1 Star formation history

The SFH of a galaxy can in principle be very complex, and it is difficult to come up with a universal model to describe the SFHs for individual galaxies. For low-mass galaxies, observations based on resolved stars (e.g. Weisz et al. 2011) have shown that the SFHs of different galaxies are quite similar over most of the cosmic time, while differences are only seen in the recent few Gyrs. These observations also indicate that low-mass galaxies generally had enhanced star formation in the early universe ($z > 1$) where they formed more than half of their stars, and that some of them have gone through complex star formation histories during the recent 1 Gyr. Such two-phase star formation is also seen in empirical models such as that of Lu et al. (2015).

We model the SFH as follows. First, we include a smooth com-

ponent represented by a Γ function:

$$\Psi(t) = \frac{1}{\tau \gamma(\alpha, t_0/\tau)} \left(\frac{t_0 - t}{\tau} \right)^{\alpha-1} e^{-(t_0-t)/\tau}, \quad (2)$$

where $t_0 - t$ is the look-back time, and $\gamma(\alpha, t_0/\tau) \equiv \int_0^{t_0/\tau} x^{\alpha-1} e^{-x} dx$. The flexibility of the function allows cases where a galaxy is dominated by old stars (with both α and τ small) or dominated by younger populations (with both α and τ large). On top of this continuous SFH, we also consider an additional burst component to mimic the old stellar component in dwarf galaxies seen in resolved stars. The burst is specified by two free parameters: t_b describes when the burst occurs, and f_b specifies the relative fraction of stellar mass formed in the burst. Thus we consider the following two SFH model types:

- Γ model: SFH given by equation (2);
- $\Gamma+B$ model: SFH given by equation (2) plus a burst.

We test the validity of these two forms of SFH using mock spectra generated from theoretical SFHs from the empirical model of Lu et al. (2015). To do this, we first convolve the theoretical SFHs with the E-MILES SSPs to obtain the corresponding noise-free composite spectra. Different levels of Gaussian noise are then added to the spectra to mimic real observations. An example of fitting such a mock spectrum with SNR=40 is shown in Fig. 1. Note that, in Fig. 1 and other figures, the burst component is represented by a Gaussian peak with finite width, even though it is modelled as a single SSP in the fitting. As one can see, although both the Γ and $\Gamma+B$ models can give a reasonable fit to the mock spectrum, the former fails to recover the input SFH. On the other hand, the $\Gamma+B$ model has the flexibility to recover the early burst component, although the exact burst time is not reproduced. For comparison, we also show the result obtained using both the optical spectrum and $(g - K)$ colour to constrain the model (see §3.2). In this case the recovered SFH (the yellow curve) closely matches the input SFH, with approximately the same burst strength and time. Fig. 2 shows another example in which the mock SFH does not contain any significant burst. Here the inclusion of a burst component in the model and the NIR photometry in the constraint does not lead to any significant changes in the inferred SFH, as the Γ function already has the flexibility to approximately describe this kind of SFHs.

To compare the true to the estimated physical properties, we analyze 2,000 such mock spectra randomly chosen from the empirical models of Lu et al. (2015) which SNR ranging from 10 to 70. The differences in the mass fraction of the old stellar population (with stellar age > 8 Gyrs) between the best-fit and input SFHs are shown in Fig. 3. It is seen that, the Γ model systematically underestimates the mass fraction of the old population, regardless of the SNR, while the $\Gamma+B$ model can well recover the input old fraction. In addition, including NIR photometry as an additional constraint can improve the accuracy of the derived mass fraction, especially when the SNR is low. Although these test results are for ideal cases, where the SSPs are assumed to describe the real stellar populations perfectly, they do indicate that $\Gamma+B$ model provides an unbiased description of the various SFHs of low-mass galaxies predicted by the empirical model.

In what follows, we will apply these two SFH models to MaNGA spectra and examine whether the data prefer Γ or $\Gamma+B$, and how model inferences are affected by the assumption of SFH model.

³ <http://miles.iac.es/>

⁴ <http://www.oa-teramo.inaf.it/BASTI>

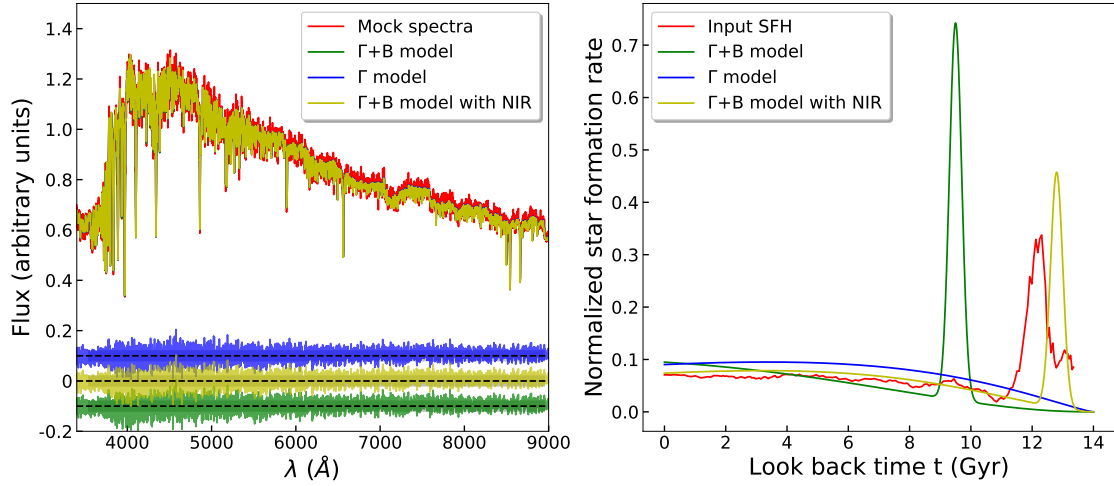


Figure 1. An example of fitting mock spectra with different SFH models. The red line in the right panel shows the SFH used to generate the mock spectrum. White noise is added to the mock spectrum so that $\text{SNR}=40$. Blue and green lines are the best-fit results to the mock spectrum from 3800\AA to 8900\AA using the $\Gamma+B$ and Γ SFH models, respectively, while the yellow line is the best-fit result of the $\Gamma+B$ model using the optical spectrum plus the $(g-K)$ colour. Residuals of the best-fit spectra are shown at the bottom of the left panel, with zero points of the blue and green lines shifted by ± 0.1 , respectively.

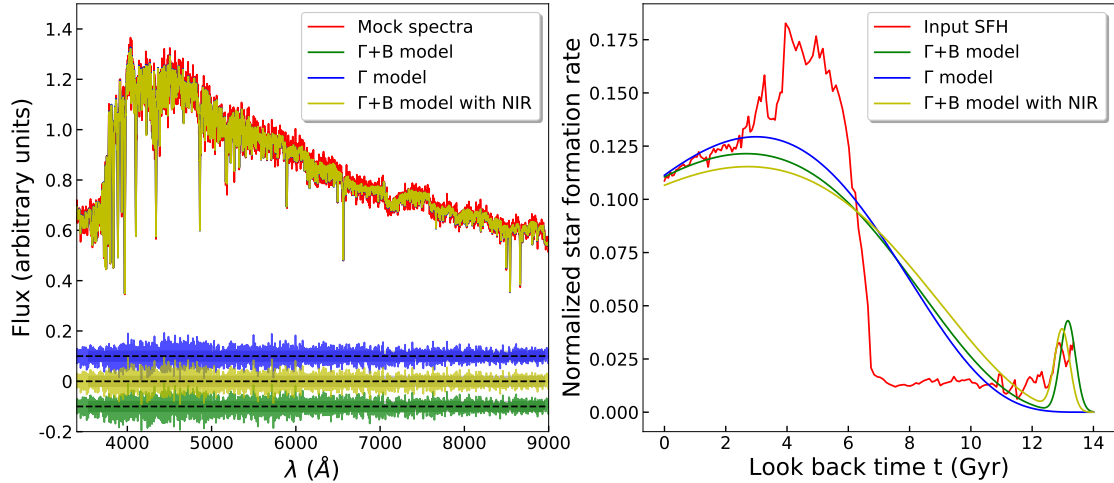


Figure 2. An example similar to Fig. 1, but for a mock SFH that does not contain a significant early burst.

3.1.2 Dust attenuation

Dust attenuation can also affect the inferred SFH. Since dust absorption is more significant at shorter wavelengths, a stellar population that contains more dust can mimic an older and/or more metal-rich population, producing the well known age-metallicity-dust degeneracy. Thus, dust attenuation has to be properly taken into account in order to make unbiased inferences from the observed spectra. In practice, dust attenuation is usually treated as an additional model parameter specifying the attenuation curve assumed. For star-forming galaxies, the Calzetti Law (Calzetti et al.

2000) is widely used. For galaxies with complex stellar populations, the two-component dust model of Charlot & Fall (2000) may be adopted to account for the difference in dust attenuation between star burst clouds (stellar populations younger than 10 Myr) and older stellar populations. As different attenuation curves are very similar to each other in the optical and NIR bands, we follow Charlot & Fall (2000) and use a single optical depth parameter to describe the attenuation of the stellar population in a galaxy.

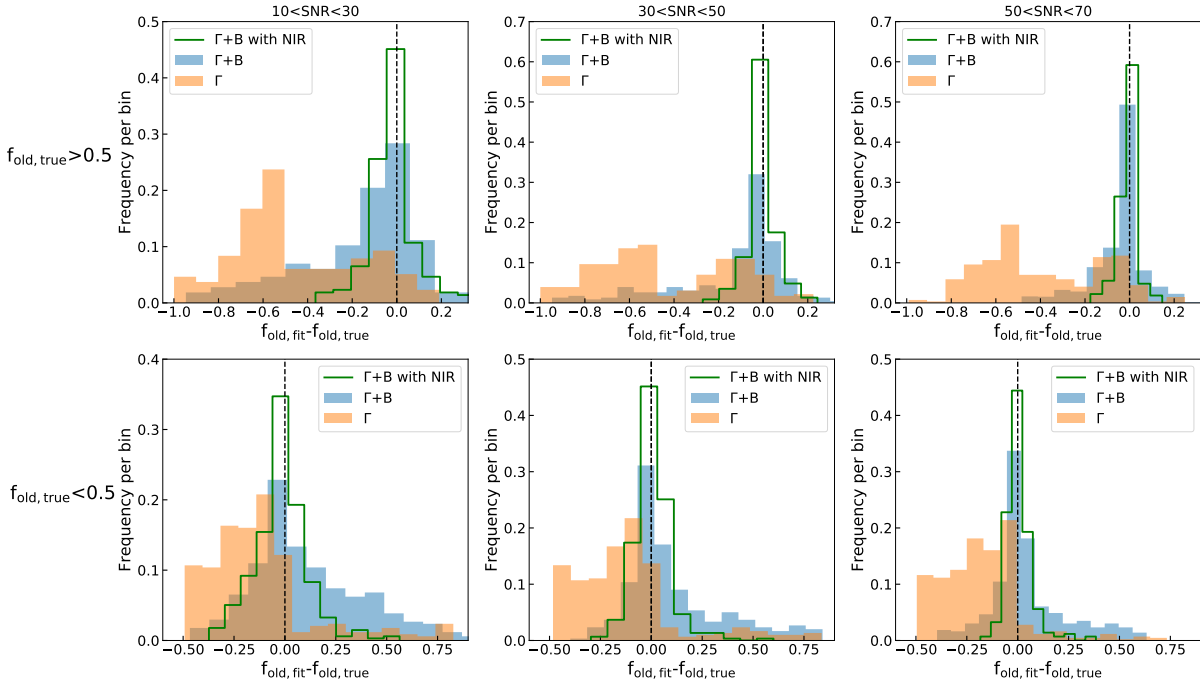


Figure 3. The distribution of the difference in the mass fraction of the old stellar population (defined to be stars with ages larger than 8 Gyrs) between the best-fit model and the input SFH. The three columns are results for mock spectra with different levels of SNR, as indicated. Upper panels are results from mock spectra with high fraction (>0.5) of old stellar populations (>8 Gyr), similar to the one shown in Fig. 1, while the lower panels are for those with a lower fraction (<0.5) of old stars, similar to the one shown in Fig. 2. The three histograms are results obtained from the $\Gamma+B$ and Γ SFH models using only the optical spectra and from the $\Gamma+B$ model using the optical spectra plus the $(g-K)$ color, respectively. Histograms are normalized to 1 over the adopted bins.

3.1.3 The implementation of BIGS

In complex problems, such as the spectrum fitting problem addressed here, the likelihood function can be complicated and may not be represented by simple analytical functions. One thus needs an efficient sampling method to sample the posterior distribution. In addition, as the Bayesian evidence ratio involves integration in high-dimensional space, an effective numerical method is also needed to evaluate it. BIGS adopts a Bayesian sampler, MULTINEST (Feroz et al. 2009, 2013), which uses the nest sampling algorithm to estimate the Bayesian evidence, and gives the posterior distribution as a by-product.

Briefly, BIGS works as follows. For each data spectrum, we pre-process it using pPXF and obtain the velocity distribution of the source. We then convolve our template spectra with a Gaussian that accounts for both the instrumental resolution and velocity dispersion of stars. The data spectrum and the templates are then provided to BIGS. Using the prior distribution of model parameters, BIGS uses MULTINEST to generate a proposal parameter vector for the spectral synthesis model. These parameters, which specify the SFH, metallicity and dust attenuation of the stellar population, are used to generate a model spectrum to be compared with the data spectrum to predict the corresponding likelihood. The likelihood is returned to the MULTINEST sampler, which makes a decision to accept or reject the proposal on the basis of the posterior probability and generates a new proposal for the model parameters. The loop continues until a convergence criterion is reached. Once

converged, the posterior distribution of model parameters, together with the Bayesian evidence, are stored for statistical analyses of the model.

3.2 The fitting procedure

We compare spectra predicted by the E-MILES SPS model to the observed MANGA spectra to infer the SFHs of the low-mass galaxies using the procedure described below. To begin with, we mask some of the spectral regions to ensure the validity of the fitting. For example, we mask the observed continua in the wavelength range 6800–8100 Å, as difficulties are commonly found in fitting the observed continua in this wavelength range, either due to issues in flux calibrations in the templates, residual telluric absorption, or even flux calibrations in the data (see Zhou et al. 2019 for more discussions). In addition, as the E-MILES templates do not contain the youngest stellar population (<0.06 Gyr), we also mask the very blue end of the spectra (<3800 Å) in the fitting.

To take into account effects of stellar kinematics and instrumental resolution, we first use the software pPXF to pre-fit the data spectra. This pPXF fitting returns an effective velocity dispersion, σ_{ppxf} , which contains all factors that contribute to spectral broadening, such as errors in the measurements of stellar velocities, intrinsic dispersion, and instrumental resolution. This effective velocity dispersion is then used to convolve with the E-MILES template spectra to generate artificially broadened templates that are used

Table 1. Priors of model parameters used to fit galaxy spectra

Parameter	description	Prior range
$\log(Z/Z_\odot)$	Metallicity	$[-2.3, 0.2]$
τ	SFH parameter in Eq. (2)	$[0.0, 10.0]$
α	SFH parameter in Eq. (2)	$[0.0, 20.0]$
τ_v	Dust optical depth at 5500 Å	$[0.0, 2.0]$
f_{burst}	relative fraction of old populations	$[0.0, 1.0]$
$\log(Z_{\text{burst}}/Z_\odot)$	Metallicity of the old population	$[-2.3, 0.2]$
A_{burst} (Gyr)	Age of the old population	$[8.0, 14.0]$

to compute the synthesised spectra to be compared with the corresponding data spectra. In this step, apparent emission lines in the spectra are also identified, and masked out in subsequent analyses.

After this pre-processing, we first normalise the model and data spectra in the wavelength window 4500 – 5500 Å and then send them to BIGS. BIGS runs the fitting loop as described in §3.1.3, assuming a flat prior and a χ^2 -like likelihood function. In the fitting that uses only the MaNGA spectra, the likelihood function is defined as

$$\ln L(\theta) \propto - \sum_{i,j=1}^N (f_{\theta,i} - f_{D,i}) (\mathcal{M}^{-1})_{ij} (f_{\theta,j} - f_{D,j}) \quad (3)$$

where N is the total number of wavelength bins, f_θ and f_D are the flux predicted from the parameter set θ and that of the data spectrum, respectively, and $\mathcal{M}_{ij} \equiv \langle \delta f_{D,i} \delta f_{D,j} \rangle$ is the covariance matrix of the data. For spectra that have UKIDSS observations, we use the following definition:

$$\ln L(\theta) \propto - \sum_{i,j=1}^N (f_{\theta,i} - f_{D,i}) (\mathcal{M}^{-1})_{ij} (f_{\theta,j} - f_{D,j}) - \frac{(K_\theta - K_D)^2}{\sigma_K^2} \quad (4)$$

where K_θ and K_D are the $(g - K)$ colour predicted from the parameter set θ and that from the data, respectively. The uncertainty in the $(g - K)$ colour is denoted by σ_K . In general, it is difficult to model σ_K . The value of σ_K is related to the accuracy of UKIDSS photometry, which has an uncertainty of less than 2% in the K band (Dye et al. 2006). In addition, σ_K should also include the relative flux variation between the MaNGA stacked spectra and the NIR photometry, which is hard to model. To minimize such influence, we only select galaxies with $\Delta(g - r) < 0.05$ between the MaNGA and UKIDSS archive data. In this case, our test shows that setting $\sigma_K = 0.02$ is appropriate to describe the constraints from the NIR observation. We list all the fitting parameters in Table 1, together with their prior distributions (assumed to be flat).

4 RESULTS

4.1 Bayesian model selection

Our goal is to investigate the existence or absence of an old stellar population in low-mass galaxies. To this end, we fit the stacked spectra (each being a stack of pixels within the effective radius of a galaxy) of individual galaxies with the two SFH models, $\Gamma+B$ and the Γ , while keeping all other parts of the model intact. We first examine if the data shows a preference for one of the two models. As described above, the Bayesian evidence ratio provided by BIGS can serve as a discriminator between different model families. Fig. 4 shows the evidence ratio between the two models, $\ln(E_{\Gamma+B}/E_\Gamma)$,

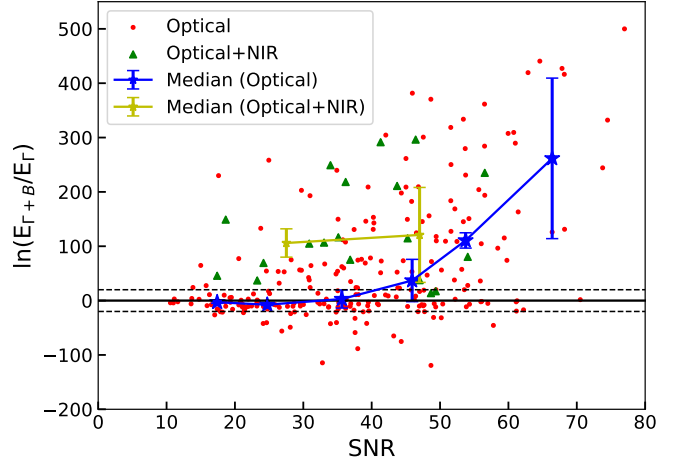


Figure 4. The evidence ratio between the $\Gamma+B$ SFH and the Γ SFH as a function of SNR of the stacked spectra. Each red dot stands for the result of a MaNGA galaxy obtained by fitting its stacked spectrum. Blue stars are the median values in five SNR bins and are linked by a blue line. Each of green triangles stands for the result obtained from fitting both the MaNGA stacked spectrum and the $(g - K)$ (see 4.3). Yellow stars are the median values in two SNR bins and are connected by a yellow line. The black solid line denotes $\ln(E_{\Gamma+B}/E_\Gamma) = 0$ while the two black dashed lines, $\ln(E_{\Gamma+B}/E_\Gamma) \pm 20$, mark the limits for significant preferences for the $\Gamma+B$ model and the Γ model, respectively. Error bars are obtained from the jackknife resampling method.

obtained from the stacked spectra, as a function of the signal-to-noise ratio (SNR) of the stacked spectra. The median values in five SNR bins are shown as blue stars to demonstrate the average trends. To estimate the statistical uncertainty, the galaxy sample is randomly divided into 20 sub-samples, and 20 different jackknife copies are generated from these sub-samples by eliminating one of the 20 sub-samples. The variances among the median values of the 20 jackknife copies are shown in Fig. 4 as the error bars.

Fig. 4 shows clearly that the median value of the evidence ratio increases with increasing SNR. At $\text{SNR} \sim 40$, the evidence ratio reaches the value $\ln(E_{\Gamma+B}/E_\Gamma) > 20$ that indicates a clear preference for the $\Gamma+B$ model. This indicates that the SFHs of these low-mass galaxies are more likely a composite of two distinct stellar components than a single component. Although the young stellar component may dominate the luminosity and makes the galaxies blue, the faint old stellar component that formed early may contribute significantly to their total stellar masses, as we will quantify next.

4.2 The stellar populations in low-mass galaxies

4.2.1 The star formation history

We first obtain the best-fit SFH for each galaxy from the posterior distribution, and plot the cumulative SFH in Fig. 5. Results are shown separately for central and satellite galaxies, using the central/satellite classification from Galaxy Environment for MaNGA Value Added Catalog (GEMA-VAC, Argudo-Fernández et al. 2015). This VAC uses the group catalogue of Yang et al. (2007) to separate MaNGA galaxies into centrals and satellites. The average cumulative SFH are shown as lines, with shaded re-

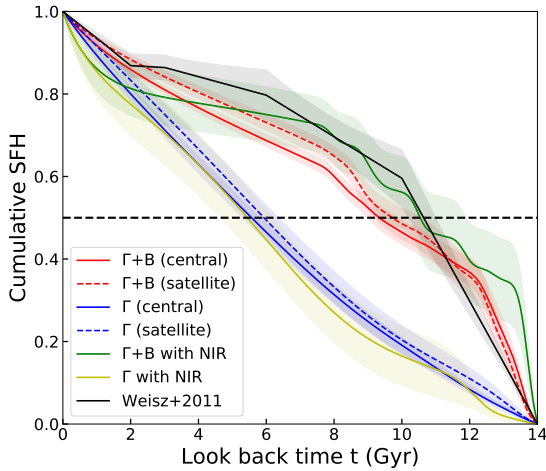


Figure 5. The cumulative SFH inferred from the posterior distribution constrained by the stacked spectra of different galaxies within $1R_e$. Red lines are from the best-fit $\Gamma+B$ model, while blue lines are from the Γ model SFH. Solid and dash lines are mean results for central and satellite galaxies, respectively. The shaded region around each line represents the error of the mean SFH, estimated from the jackknife resampling method. The result of Weisz et al. (2011) is shown as a black solid line. Results obtained from the MaNGA stacked spectra plus the $(g-K)$ colour (see 4.3) using the $\Gamma+B$ model SFH and the Γ model SFH are shown with green and yellow lines, respectively. The horizontal black dashed line marks the position of half of the total star formation.

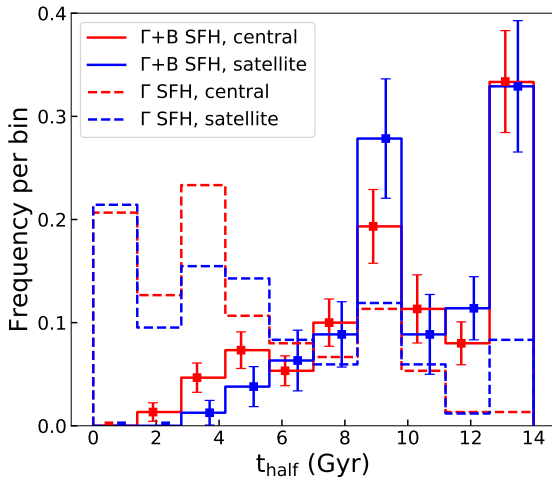


Figure 6. The distribution of the half mass formation time inferred from the best-fit SFH models. Red and blue histograms show the results of central and satellite galaxies, respectively. Solid and dash histograms are obtained using the $\Gamma+B$ SFH and the Γ SFH, respectively. Error bars, only shown for the $\Gamma+B$ SFH, are obtained from the jackknife resampling method. Each histogram is normalized to 1 over all the bins used.

gions indicating the errors estimated from the jackknife resampling method.

Our results derived from the $\Gamma+B$ model (red lines) indicate that low-mass galaxies on average formed about half of their stellar masses more than 8 Gyrs ago, which may be associated with the starburst events observed in extreme emission line galaxies detected in the CANDELS survey (van der Wel et al. 2011). As a comparison, the black line shows the cumulative SFHs of local dwarf galaxies in the mass range $10^8 - 10^9 M_\odot$ obtained from resolved stars by Weisz et al. (2011). It is remarkable that the results obtained from the $\Gamma+B$ model are in good agreement with that of Weisz et al. (2011). In contrast, the results obtained from the Γ model (blue lines) indicate that most of the stellar mass in low-mass galaxies formed recently. This discrepancy is expected. Since an old stellar population is much fainter than the young population of the same mass, a model that is not sufficiently flexible to allow for the existence of both populations will miss the old population. As shown in §4.1, this limitation of the Γ model weakens its ability to describe the true SFH, which leads to the smaller Bayesian evidence in comparison to the $\Gamma+B$ model in fitting spectra of sufficiently high SNR. In what follows, we will focus on the results derived from the $\Gamma+B$ model and use them to compare with those in the literature; results from the Γ model will be presented only when necessary.

Environmental effects can also be seen from Fig. 5, in that satellite galaxies appear to form their stars slightly earlier than central galaxies. This is expected, as low-mass satellites may have their star formation quenched by environmental effects of their host halos (e.g. van den Bosch et al. 2008; Peng et al. 2012).

In addition to the cumulative SFH, we also derive the half-mass formation time, t_{half} , defined as the look-back time when a galaxy forms half of its final stellar mass, from the best-fit SFH models and plot the results in Fig. 6. Again, GEMA-VAC is used to divide our sample into centrals (red) and satellites (blue). For the $\Gamma+B$ model, as one can see, t_{half} varies from 2 Gyr ago to 12 Gyr, with a broad peak at about 9 Gyr. In contrast, t_{half} in the Γ model is smaller on average, ranging from zero to 12 Gyr with a broad peak at about 4 Gyr.

In addition, for the $\Gamma+B$ model, there is an excess of the t_{half} for central galaxies at around 5 Gyr comparing to satellites. This weak peak indicates a secondary star formation episode, as is expected from the "gappy" star formation history found by Wright et al. (2019). These results are in rough agreement with those of Kauffmann (2014), who found that the distribution of t_{half} for low-mass galaxies, derived from analysis of Dn4000 and H_{δ_A} absorption features, is quite broad and shows double peaks.

We note that there is a significant peak in the distribution of t_{half} at around 13 Gyr. However, our extensive test shows that this peak may not be real. We only use a single SSP to describe the burst in the early-Universe, and the age of the burst is confined to be within the age of Universe. As the spectra of old SSPs are insensitive to the age (e.g. Bruzual & Charlot 2003), a galaxy with an early starburst that contributes more than half of its stellar mass could have the best-fit t_{half} at the edge of the prior. By setting the prior age range to be the maximum age of the SSP model, which is 18 Gyr for the EMILES model, we found that some best-fit ages would move out of the previous boundary, and the peak at 13 Gyr would disappear. These results indicate that the current model is not able to describe the ages of old stellar populations accurately. Because of this limitation, the exact ages of the old population predicted by the model should be treated with caution. We emphasise, however,

that this limitation does not affect the conclusion that those galaxies contain large fractions of old stars.

4.2.2 The old stellar populations

Fig. 7 shows the mass fraction of stars in three populations, old (>8 Gyr), middle-age (4–8 Gyr), and young (<4 Gyr). We show the results for central and satellite galaxies separately, and for both the $\Gamma + B$ (upper panels) and Γ (lower panels) models for comparison. For the $\Gamma + B$ model, the fractions are $\sim 60\%$, 20% and 20% for the three populations, and are quite similar for central and satellites. For the Γ model, the fractions are $\sim 30\%$, $\sim 30\%$ and $\sim 30\%$. Therefore, the Γ model significantly underestimates the fraction of old stars while overestimating the young population fraction in comparison with the $\Gamma + B$ model. For comparison, we show the results obtained from the resolved observation of Weisz et al. (2011) as black dots. Although the resolved data is sparse, there is a good match of the data with the distribution inferred from the $\Gamma + B$ model but a significant mismatch with the inferences of the Γ model, indicating again that the inclusion of an early burst is the minimal requirement to explain the stellar population in low-mass galaxies. Note that the amount of stars in the middle age (4–8 Gyr) is relatively small both in the prediction of the $\Gamma + B$ model and in the result based on resolved stars. This is not well reproduced in hydrodynamic simulations (Digby et al. 2019), suggesting that the observational data can provide important constraints on the formation and evolution of low-mass galaxies.

4.2.3 Radial dependence

The spatially resolved spectra provided by MaNGA allow us to investigate the SFHs in different parts of the galaxy. Here we use MaNGA spectra stacked in four radial bins, $[0.0 - 0.3)R_e$, $[0.3 - 0.7)R_e$, $[0.7 - 1.2)R_e$, and the entire galaxy with all spaxels, to investigate how the SFH varies with radius. We derive the average SFH from the radially stacked spectra using the $\Gamma + B$ model. Fig. 8 shows the cumulative distribution of the SFH obtained at the four radial intervals, for central and satellite galaxies separately. As one can see, satellites form their stars slightly earlier than centrals and this is true for all radii. In addition, the figure shows that stars in the innermost part of a low-mass galaxy on average formed earlier by ~ 1 Gyr than those in the outer part.

Fig. 9 shows the half-mass formation look-back time, t_{half} , for different radial bins obtained using the $\Gamma + B$ model. The half mass formation time obtained for different radial bins varies from 2 Gyr ago to 12 Gyr, with a broad peak at about 8 Gyr. This peak is seen at all radii, for both central and satellite galaxies. This indicates that the old stellar population exists not only in the central part of galaxy, but spreads over the entire galaxy, making a significant contribution to the total stellar mass. We note that, for central galaxies and for all the galaxies as a whole, all the regions present a long tail in the t_{half} distribution at $t_{\text{half}} < 5$ Gyr, indicative of recently-formed young populations. In contrast, this long-tail at < 5 Gyr is absent in the innermost and intermediate-radius regions of the satellite galaxies, indicating that the star formation in the inner region of satellites has been quenched earlier than their outer region.

4.3 Constraints from NIR

The results presented above are obtained using MANGA optical spectra as constraints. The SSP templates from the E-MILES model

in fact have wavelength coverage from 1600 \AA to 5 \mu m . Thus, these SSP templates allow us to predict the fluxes in both optical and NIR bands once a set of model parameters are given. By comparing the predicted colour with observations, we can get additional constraints on the stellar population of galaxies. Compared to spectroscopic observations, broad band measurements are much easier to make, although they may lose some spectral information. As old stars emit the majority of their light in NIR, a combination of optical spectra and NIR photometry is expected to provide better constraints on the SFH model which includes early star formation. In this subsection, we demonstrate this using the combination of UKIDSS K -band flux and MaNGA optical spectrum.

The fitting example of mock spectra in Fig. 1 illustrates the improvement of the derived SFH when $(g - K)$ colour is included in the fitting. As a real example, Fig. 10 shows the fitting results for MaNGA 9876-3703, one of the galaxies in our sample. From the optical image shown in the left panel, one can see that this galaxy is quite blue, indicative of ongoing star formation. Indeed, if we assume a simple Γ model to fit its MaNGA spectra, the SFH obtained is dominated by recent star formation, with almost no population older than 8 Gyr, as shown by the blue lines. In contrast, the use of the $\Gamma + B$ model reveals the existence of a significant old stellar population. However, neither of the two constrained models can recover perfectly the observed $(g - K)$ colour for this galaxy. Using the posterior distribution of the model parameters obtained from the E-MILES templates, the best-fit of the Γ and $\Gamma + B$ models predicts $(g - K) = 2.08$ and $(g - K) = 2.22$, respectively, while measurement from WSA is $(g - K) = 2.43$. These results indicate that the lack of constraints from NIR may still lead to biased inferences of the stellar population, even if a proper SFH is assumed.

In order to check the effects of including NIR photometry, we implement a new set of fitting, adopting the modified likelihood function described by equation (4). The results obtained for MaNGA 9876-3703 are plotted in Fig. 10 with solid lines. The inclusion of the $(g - K)$ colour changes the fitting result of the $\Gamma + B$ model significantly, in that the fraction of the old population increases significantly. The predicted $(g - K)$ colour is 2.38, very close to the observed value. In contrast, the result obtained from the Γ model is not affected as much by the inclusion of the NIR data, with $(g - K) = 2.27$, which is still substantially too blue.

We apply the same fitting to all the 19 galaxies that have UKIDSS NIR photometries. The green triangles in Fig. 4 show the evidence ratio between the $\Gamma + B$ and the Γ models as a function of SNR of the stacked spectrum. Yellow stars are the median of the values in two SNR bins, divided at $\text{SNR} = 40$. Compared to the red dots that only use the MaNGA stacked spectra, there is a significant increase in the evidence ratio, indicating an increase in the ability of discriminating the two SFHs.

The green and yellow lines in Fig. 5 show the cumulative SFHs for the NIR sample obtained from the best-fit $\Gamma + B$ and Γ model, respectively. Compared to the red lines that show results using MaNGA spectra alone, the result obtained with the $\Gamma + B$ model including the NIR data shows a significant increase in the stellar mass formed 8 Gyr ago, although the uncertainty is large owing to the limited sample size. In contrast, the result obtained by the Γ model does not change much.

In Fig. 11, we compare the half mass formation times and the fractions of old (>8 Gyr) population derived from optical-only and optical plus NIR data. The inclusion of the NIR constraint tends to predict an earlier formation time in these galaxies, or equivalently, a higher fraction in the old population. These results confirm the existence of old populations in low-mass galaxies. They also sug-

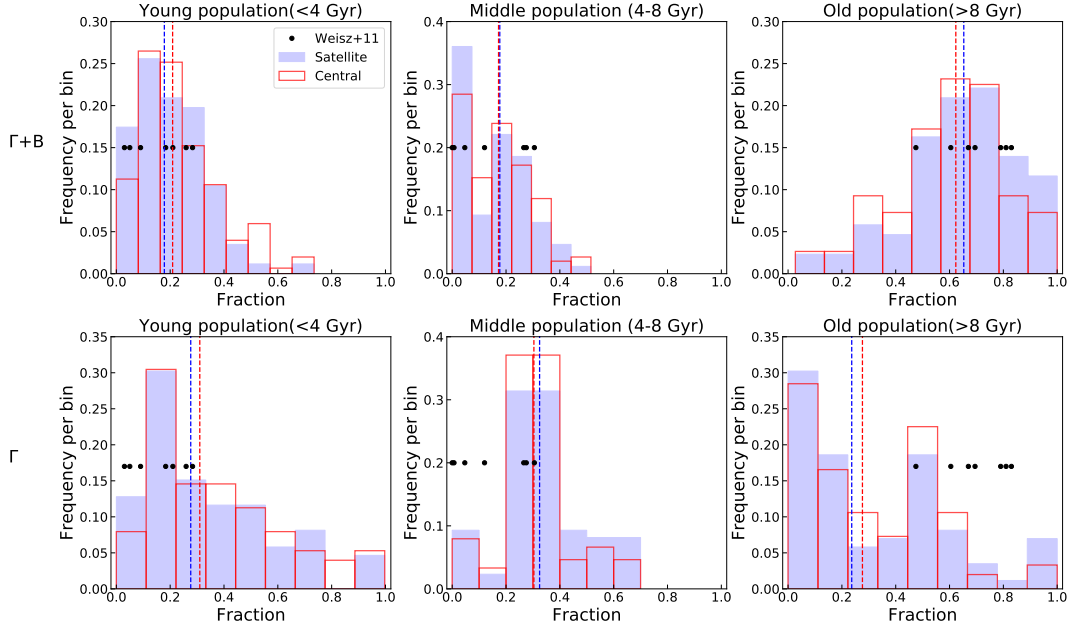


Figure 7. The distribution of the mass fraction of stars in the old (>8 Gyr, left), middle-age (4–8 Gyr, middle), and young (<4 Gyr, right) stellar populations. Top panels are results obtained from the $\Gamma+B$ SFH model, while bottom panels are from the Γ model. Red and blue histograms are for centrals and satellites, respectively, with dash lines showing the median values. Black dots are results of Weisz et al. (2011). All histograms are normalized to 1 over the bins used.

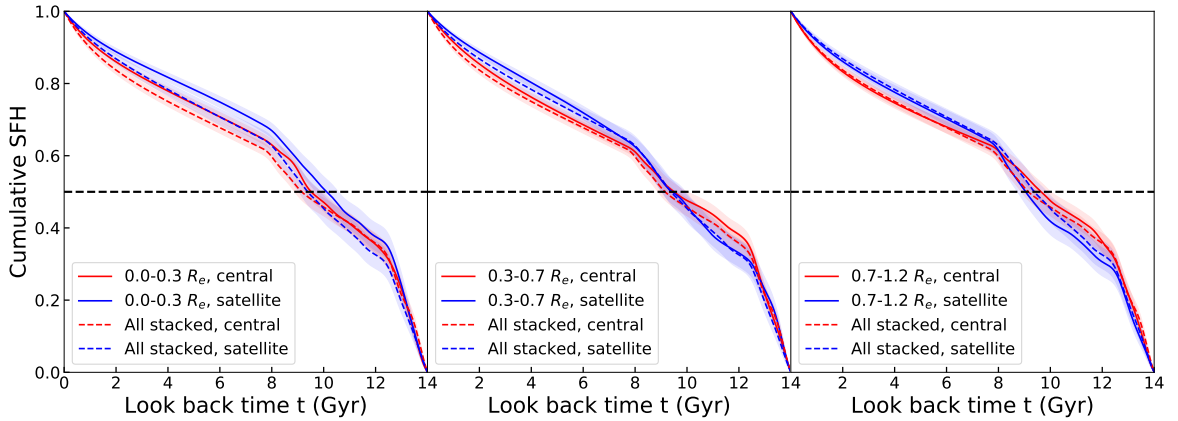


Figure 8. The cumulative SFH inferred from the best-fit $\Gamma+B$ model. Solid lines in all three panels show results for radial bins $[0.0-0.3]R_e$, $[0.3-0.7]R_e$, and $[0.7-1.2]R_e$, respectively. As a reference, results of stacking spaxels of the entire galaxy are shown by dash lines in all panels. Red and blue lines are for central and satellite galaxies, respectively. The shaded region around each line represents the error of the mean SFH, estimated from the jackknife resampling method. The horizontal black dashed line marks the position of half of the total star formation.

gest that the burst fraction inferred from the optical spectra alone may underestimate the true fraction.

However, we should point out that those results also raise a concern. The tension between the predictions based on optical spectra and NIR photometry indicates that the model adopted may not be sufficiently general. To examine this problem in more detail, we apply the posterior predictive check method to the sample of 19 galaxies with NIR photometry. The detail is presented in

the Appendix A. In general, we find that the model is often over-constrained by the optical spectra, so that the posterior predictive distribution (PPD) of the NIR photometry is very narrow and the observed NIR data is almost always rejected by the posterior predictive check (PPC). In Bayesian statistics, the inferences obtained from data apply only to the model (hypothesis) assumed. If the model is not general enough to accommodate all the information in the data, inferences can still be made for the assumed model. In

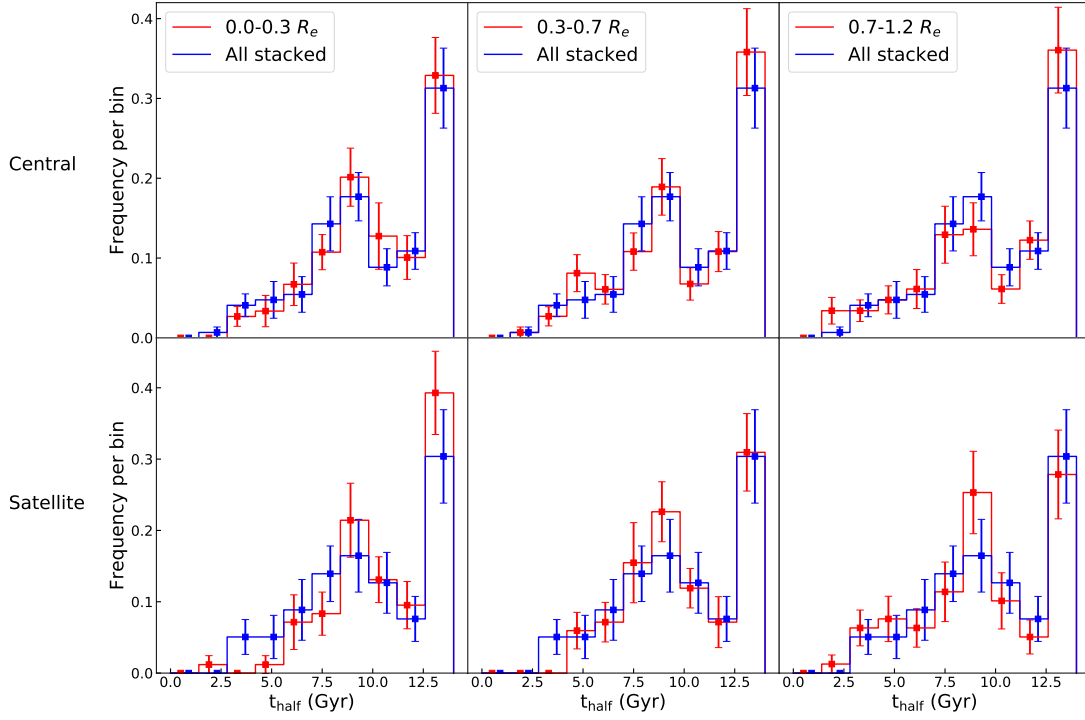


Figure 9. The distribution of the half mass formation time inferred from the best-fit Γ +B model. The three columns are for radial bins of $[0.0-0.3]R_e$, $[0.3-0.7]R_e$, and $[0.7-1.2]R_e$ respectively, with results from the entire galaxy shown in blue as a reference. Top and bottom rows are for central and satellite galaxies, respectively. Error bars are obtained from the jackknife resampling method. Histograms are normalized to 1 over the bins adopted.

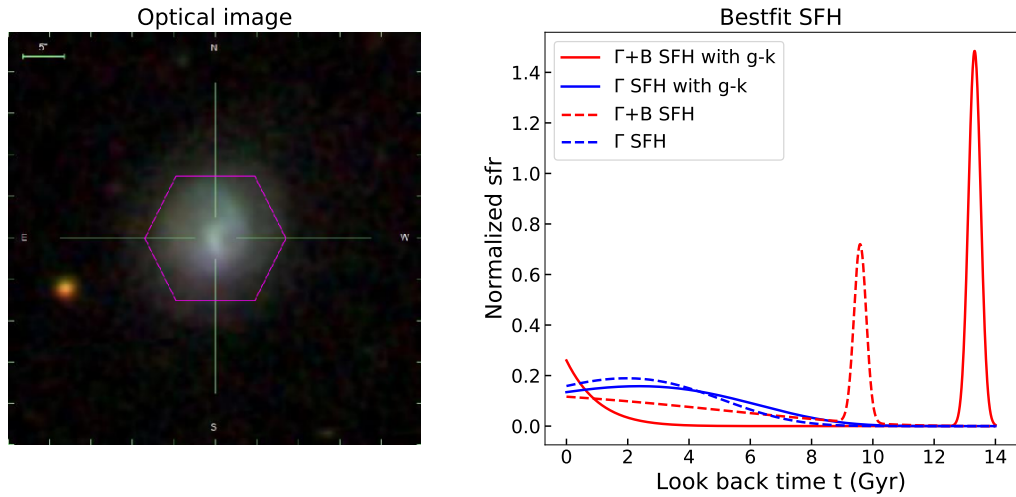


Figure 10. An example showing the changes in the inferred SFH by including UKIDSS NIR colour in the fitting. The left panel shows the optical image of this galaxy, and the right panel shows the best fit SFHs from different models. Red and blue lines show the results from the Γ +B and Γ models, respectively. Dash lines are results from the stack spectra from MaNGA, while solid lines are results that include the $(g - K)$ colours.

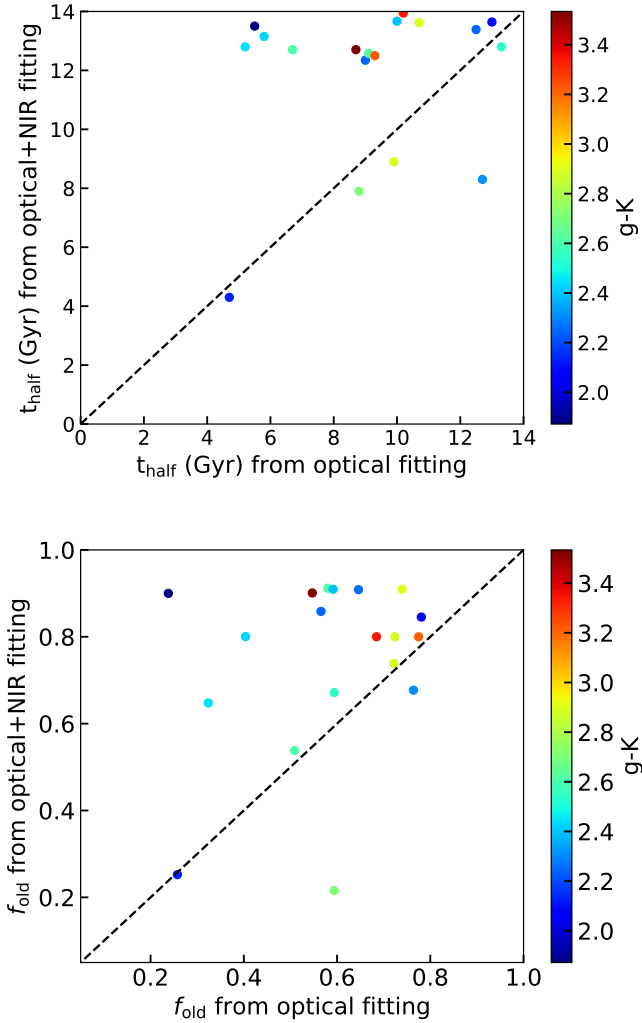


Figure 11. Comparison of the half mass formation time (top) and the fraction of old population (bottom) between fitting only the MaNGA stacked spectra (horizontal axis) and fitting both optical spectra and NIR photometry (vertical axis), colour coded by the $(g - K)$ colour of galaxy.

this case, it is important to use all available data to obtain a balance between different constraints.

In summary, the inclusion of NIR photometry confirms and strengthens the conclusion that low-mass galaxies contain a large fraction of old stars. However, one should keep in mind that the uncertainties in the spectral synthesis model may affect the details of our inferences.

5 UNCERTAINTIES

The results obtained above are based on the analysis of MaNGA spectra and UKIDSS NIR photometry with the use of BIGS. We adopt the state-of-the-art SPS model based on the E-MILES SSP templates, and assume two models for the SFH. In this section we examine further potential uncertainties in different parts of our analysis.

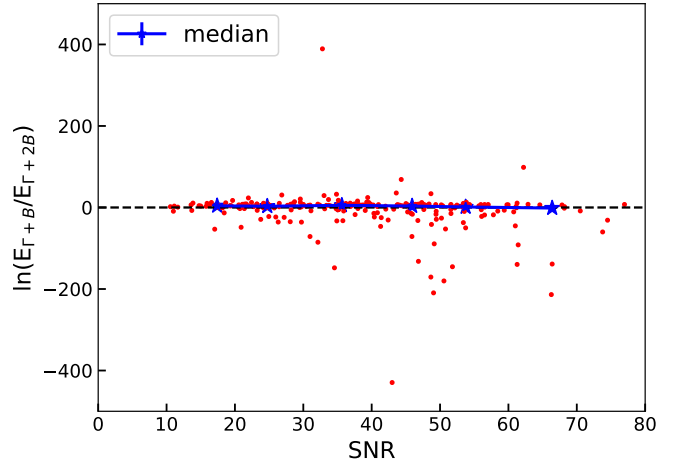


Figure 12. The evidence ratio between the $\Gamma+B$ SFH and the $\Gamma+2B$ as a function of SNR of the stacked spectra. Each red dot stands for the result of a MaNGA galaxy. Blue stars are the median values in five SNR bins, connected by a blue line. Error bars are obtained from the jackknife resampling method.

5.1 SFH models

We first examine whether or not our SFH model is sufficient to characterise the SFH of real galaxies. To this end, we first extend our SFH model by including an additional, independent burst. This model is referred to as the $\Gamma+2B$ model in what follows. Fig. 12 shows the evidence ratio between the $\Gamma+2B$ model and the $\Gamma+B$ model as a function of SNR. As one can see, only a handful of galaxies show a preference for the $\Gamma+2B$ model, and the medians of the evidence ratio do not show any systematic trend. This indicates that the data do not need the inclusion of an additional burst. Thus, given the current data quality and SPS model, our $\Gamma+B$ model may be sufficient.

However, the parametric form of SFH adopted in our analysis is still restrictive. It is interesting to see if the use of a general, non-parametric form will change our results. Non-parametric models avoid the limitation of assuming a specific functional form, but the total number of time intervals (time resolution) is usually limited to be quite small by the data. In practice, spectral analysis codes that focus on spectral fitting and stellar population parameters (e.g. age and metallicity), such as STARLIGHT (Cid Fernandes et al. 2005) and pPXF (Cappellari & Emsellem 2004), usually adopt the non-parametric approach, while codes that focus on constraining model parameters, such as CIGAL (Noll et al. 2009; Boquien et al. 2019) and BEAGLE (Chevallard & Charlot 2016), prefer the parametric approach.

As a test, here we consider a stepwise SFH model in which the SFH is described by the average star formation rates in 7 time intervals: $0 \rightarrow 0.2$, $0.2 \rightarrow 0.5$, $0.5 \rightarrow 1.0$, $1 \rightarrow 2$, $2 \rightarrow 6$, $6 \rightarrow 10$ and $10 \rightarrow 14$ Gyr. Since only the relative fraction of stars formed in each interval change the spectra shape, the model has 6 free parameters. We plot the cumulative SFH inferred from the step-wise SFH in Fig. 13, in comparison to that inferred from the $\Gamma+B$ model. The results of the two models match each other well, with a discrepancy much smaller than the inference uncertainty shown by the shaded regions. This consistency indicates that, as long as the SFH model

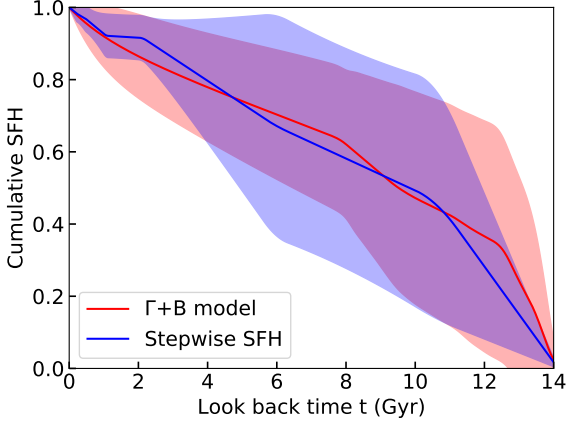


Figure 13. The cumulative SFH inferred from the best-fit $\Gamma+B$ model (red) and the stepwise SFH (blue). Lines show the mean SFHs of the sample, while shaded regions denote the scatter among the sample galaxies.

is sufficiently flexible to describe the major stellar populations, the results from our spectral fitting are robust.

5.2 SSP models

Spectral modelling is based on the linear combination of SSP templates. Thus, the accuracy and completeness of the SSP templates can influence fitting results. Unfortunately, the uncertainties of the SSP templates are not well-understood. As a test of this uncertainty, we use the BC03 model to perform a consistent check. In contrast to the E-MILES model, the BC03 SSPs are constructed with the STELIB (Le Borgne et al. 2003) empirical stellar templates. Models assuming Padova isochrones (Bertelli et al. 1994) and the Chabrier IMF are used in the comparison. The top panel of Fig. 14 shows the evidence ratio between the $\Gamma+B$ and Γ models, derived from the fitting with BC03 templates, as a function of the SNR. The trend seen here is similar to that shown in Fig. 4 although is slightly weaker.

We have also made a test using a mixture of E-MILES and BC03. In this model, the model fluxes are calculated as $F = F_{BC} \times f_{BC} + F_{EM} \times (1 - f_{BC})$, where F_{BC} and F_{EM} are the fluxes obtained from the BC03 and E-MILES templates. The relative contribution of BC03 is described by f_{BC} , which is treated as a free parameter. The evidence ratio derived from this model, shown in the bottom panel of Fig. 14, is found to lie between the E-MILES and BC03 results.

We plot the cumulative SFH inferred from the best-fit $\Gamma+B$ model using E-MILES, BC03 and the mixture of the two in Fig. 15. The underestimation of the old stellar population by the simple Γ SFH can be seen easily by comparing it with the $\Gamma+B$ SFH, regardless of the assumed SSP model. For $\Gamma+B$ SFH, the inferred shapes of the SFH from the two SSP models are in overall agreement with each other. The prediction of the mixture model falls between the two; it is closer to E-MILES at early time and becomes closer to BC03 at later time. All the models reveal the presence of an old stellar population that dominates the stellar masses, but they differ in detail in their predictions of the burst strength and age.

These differences can be caused by the different constructions of the two SSP models, such as the underlying stellar templates, the isochrones used to calculate the SSPs, and even the methods used to

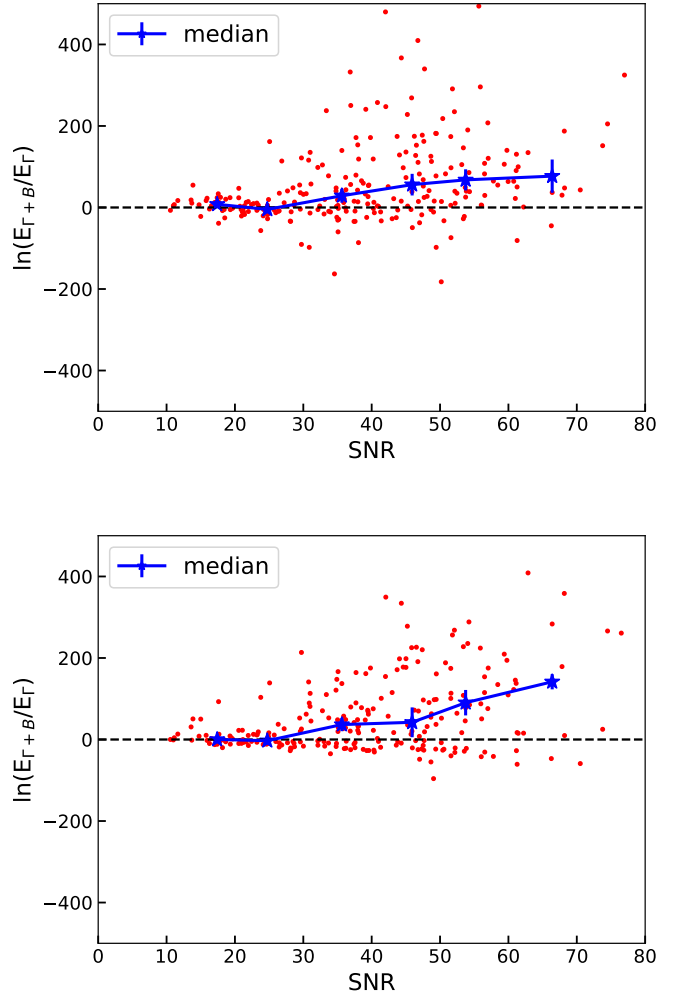


Figure 14. The evidence ratio between the $\Gamma+B$ SFH and the Γ SFH as a function of SNR of the stacked spectra, derived from the BC03 model (top panel) and the mixed model (bottom panel). Each red dot stands for the result of a MaNGA galaxy. Blue stars are the median values in five SNR bins connected by a blue line. Error bars are obtained from the jackknife resampling method.

populate stars in parameter space, but it is beyond the scope of the present paper to figure out the exact difference between the two SSP models. However, our test does show that the results obtained above are qualitatively robust against the variation of the SSP templates, but that quantitative details can be affected significantly by using different SSP models.

5.3 The NIR photometry

The accuracy of the predicted NIR photometry depends on the accuracy of the SSP templates in the NIR. For the E-MILES model, the SSPs at $\lambda > 8950 \text{ \AA}$ are constructed using the empirical IRTF stellar template (Cushing et al. 2005; Rayner et al. 2009). This treatment provides a self-consistent E-MILES SSP spectra with moderately high resolution ($\sigma = 60 \text{ km s}^{-1}$) at the NIR. In contrast, the BC03 model uses theoretical, low resolution NIR spectra of BaSel (Westera et al. 2002). This difference may affect the pre-

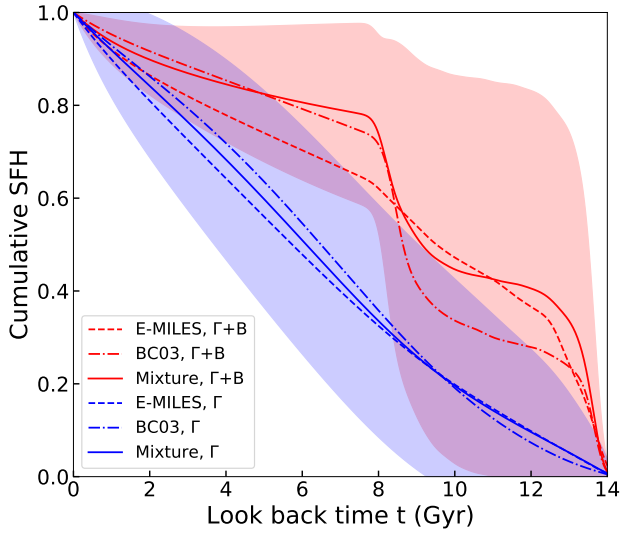


Figure 15. The cumulative SFH inferred from the best-fit SFH models using E-MILES templates (dash line), BC03 templates (dash-dotted line), and the mixed model (solid line). Lines show the mean SFHs of sample, while the shaded region shows the scatter among sample galaxies obtained from the mixed model. Red and blue colours are for the $\Gamma+B$ and Γ models, respectively.

dicted NIR photometry. To test this uncertainty, we apply the BC03 model to the sample that has both MaNGA and UKIDSS data. We plot the half mass formation look-back time, t_{half} , and the fraction of old (>8 Gyr) stellar population derived from optical only data and optical plus NIR data in Fig. 16. Comparing with the results shown in Fig. 11, we see that the two SSP models reach the same conclusion that the inclusion of NIR data enhances the significance of the old stellar population.

In addition to the BC03 model, here we mention briefly another SSP model family, the SSP model of Maraston (Maraston 2005; Maraston & Strömbäck 2011). This model was first presented in Maraston (2005) using low-resolution theoretical BaSeL stellar libraries, and an updated version using a set of stellar templates was published in Maraston & Strömbäck (2011). The Maraston model contains treatments of TP-AGB and HB stars that are different from those in E-MILES and BC03. These treatments lead to redder colours for SSPs with ages around 1 Gyr. As the dwarf galaxies studied here have quite a significant population of such ages, the difference in the predicted $(g-K)$ colour can be as large as ~ 0.15 . Unfortunately, the Maraston model cannot be compared with E-MILES. The high-resolution model, which is needed for our modeling, is based on theoretical MARCS templates that have very limited age and metallicity coverages. The models based on empirical templates have relatively wider coverage in age and metallicity, but they generally only cover the optical range. Due to these reasons, it is difficult to make a meaningful comparison with this model.

In summary, our current SPS modelling is sufficient to describe the stellar population in the galaxies studied here, and our method is in general robust against the variation in both the SSP model and the SFH model. Thus, the main conclusions we have

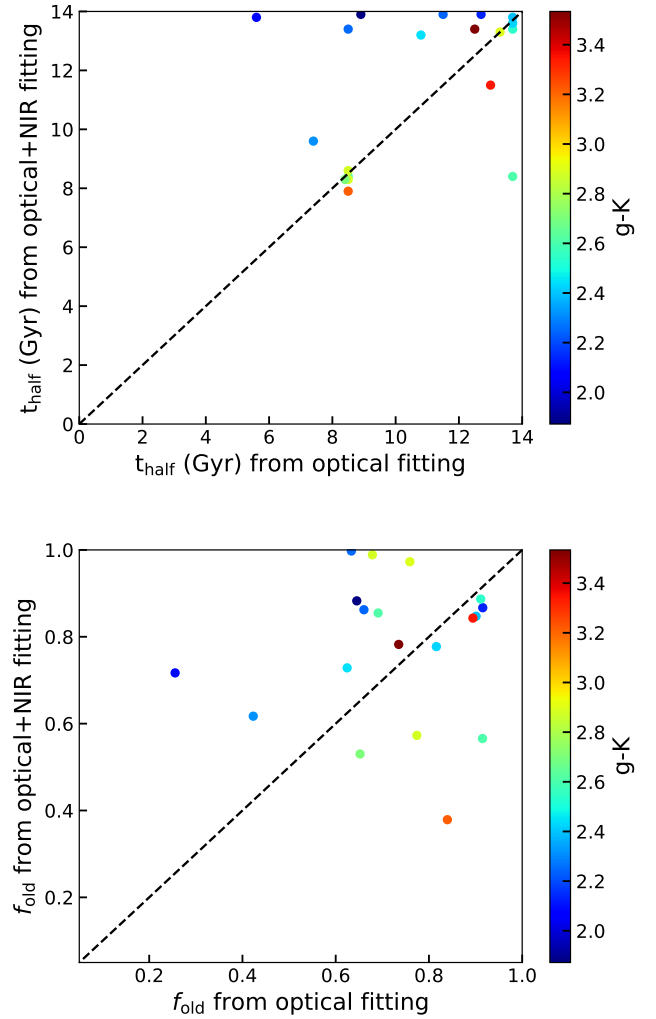


Figure 16. Comparison of the half mass formation time (top) and the fraction of old population (bottom) obtained from fitting only the MaNGA stacked spectra (horizontal axis) and fitting both optical spectra and NIR photometry (vertical axis), using the BC03 templates. Results are colour coded by the $(g-K)$ colour of the galaxy.

reached are robust, while several details (such as the SFH shape) may still require further improvements.

6 SUMMARY AND DISCUSSION

In this paper, we analyse the spectra of a sample of low-mass galaxies using the Bayesian inference code BIGS. Our sample galaxies are selected from the SDSS IV-MaNGA IFU survey, and some of the galaxies also have NIR photometry obtained from the WSA catalogue. We stack the spatially resolved spectra of each galaxy within a radius of $1.0R_e$ to obtain a representative high SNR spectrum for the galaxy. We also stacked spectra in three radial bins, $[0.0-0.3]R_e$, $[0.3-0.7]R_e$ and $[0.7-1.2]R_e$, to study possible radial variations. We analyse the stacked spectra using a full spectrum fitting approach, making use of the MaNGA spectra from 3400 Å to 8900 Å. In our analyses, we adopt state-of-the-art E-MILES SSP

templates, and assume two SFH models, the Γ and $\Gamma+B$ models to derive the stellar population properties. We use Bayesian model selection to distinguish between different models, and use the posterior distribution to constrain model parameters. Our main results can be summarised as follows:

- Based on Bayesian model selection, we demonstrate that low-mass galaxies contain an old stellar population that may be missed in results obtained from low-resolution spectra and a too restrictive model for the SFH.
- The best fit SFHs derived from the posterior distributions confirm the Bayesian model selection results that low-mass galaxies on average have formed more than half of their stellar mass at $z > 2$. The half mass formation time and the cumulative SFH from our spectra fitting of the unresolved stellar populations are in good agreement with those obtained from observations of resolved stars (Weisz et al. 2011).
- The mass fractions of the old stellar population derived from our $\Gamma+B$ model can be as high as ~ 0.7 , which is consistent with the resolved observation (Weisz et al. 2011), but inconsistent with some hydrodynamic simulations (e.g. Digby et al. 2019).
- Compared with central galaxies, satellite galaxies on average have formed their stellar mass earlier, indicating an environmental suppression of star formation in satellite galaxies. Stars in the outer regions of a galaxy are younger than those in the central part.
- We find that including the $(g-K)$ colour can further constrain the fraction of the old stellar population. The $\Gamma+B$ SFH model can reproduce the observed optical spectra and the $(g-K)$ colour simultaneously, while the Γ SFH does not have such flexibility. The predicted fraction of the old stellar population becomes larger when the $(g-K)$ colour is used as an additional constraint.
- We test potential uncertainties both in the SSP model and the SFH model, and find that our main results on the existence of an old stellar population in low-mass galaxies are robust.

Although SFHs in low-mass galaxies have been studied quite extensively, the underlying physical processes that regulate star formation are still poorly understood. For example, our results suggest that the SFH of low-mass galaxies may consist of an early star formation episode, where about half of the stellar mass was formed, followed by a secondary and more extended phase of star formation. This type of SFH is consistent with the empirical model of Lu et al. (2014), which predicts that many dwarf galaxies have experienced a phase of rapid star formation at $z > 2$. This enhanced star formation at $z > 2$ may be related to the fast accretion of dark matter halos (e.g. Zhao et al. 2003; Mo & Mao 2004) and seems to be required by the observed upturn in the low-mass end of the stellar mass function of galaxies (Lan et al. 2016), but is not predicted by many models of galaxy formation (Lim et al. 2017). In particular, the mass fractions in different stellar populations obtained from our analysis are not well reproduced by current hydrodynamic simulations (e.g. Digby et al. 2019). These suggest that the feedback effect assumed in the model to suppress star formation in low-mass halos may be too strong at high redshift. Clearly, the observational constraints on the SFH we obtain here can provide important information about the feedback processes operating in the population of low-mass galaxies.

Of all the approaches adopted to probe the SFH of low-mass galaxies, the most reliable methods are perhaps those based on resolved stars. However, such observations can be made only for a small number of nearby galaxies. In contrast, methods based on stellar population models can use a large sample of galaxies. Among the approaches based on spectral synthesis, SED fitting of

broad-band photometry (e.g. Janowiecki et al. 2017; Telles & Melnick 2018) and absorption line analysis (e.g. Kauffmann 2014) have been used to infer the SFHs of low-mass galaxies. Compared to these two approaches, our method based on full spectral fitting can in principle extract more information from the spectra. However, SED fitting has the advantage that multi-band photometry is easier to obtain. As we have shown, analysis based on spectra with limited wavelength coverage can result in biases in the inferred stellar population. Our Bayesian analysis that combines MaNGA optical spectra and NIR photometry from UKIDSS is an attempt to overcome this difficulty. As shown in §4.3, this approach is promising in probing the stellar population in low-mass galaxies, in particular in revealing the old population that may be missed in earlier investigations. However, it should also be noted that this approach is still in its early stage, and more explorations are needed to take full advantage of it. Accurate and self-consistent SSP templates are crucial for this type of analysis. As seen in §5, although variations in the SSP model generally do not change our results qualitatively, they do affect the details of inferences. Care must be taken in calibrating different observations. In the future, with improvements of our understanding about stellar spectra and of stellar spectral templates, the method and analysis proposed in this paper are expected to provide an important avenue to explore the star formation in low-mass galaxies.

ACKNOWLEDGEMENTS

This work is supported by the National Key R&D Program of China (grant No. 2018YFA0404502, 2018YFA0404503), and the National Science Foundation of China (grant Nos. 11821303, 11973030, 11761131004, 11761141012). MB acknowledges FONDECYT regular grant 1170618. G.R. is supported by the National Research Foundation of Korea (NRF) through Grants No. 2017R1E1A1A01077508 and 2020R1A2C1005655 funded by the Korean Ministry of Education, Science and Technology (MoEST), and by the faculty research fund of Sejong University.

Funding for the Sloan Digital Sky Survey IV has been provided by the Alfred P. Sloan Foundation, the U.S. Department of Energy Office of Science, and the Participating Institutions. SDSS-IV acknowledges support and resources from the Center for High-Performance Computing at the University of Utah. The SDSS web site is www.sdss.org.

SDSS-IV is managed by the Astrophysical Research Consortium for the Participating Institutions of the SDSS Collaboration including the Brazilian Participation Group, the Carnegie Institution for Science, Carnegie Mellon University, the Chilean Participation Group, the French Participation Group, Harvard-Smithsonian Center for Astrophysics, Instituto de Astrofísica de Canarias, The Johns Hopkins University, Kavli Institute for the Physics and Mathematics of the Universe (IPMU) / University of Tokyo, Lawrence Berkeley National Laboratory, Leibniz Institut für Astrophysik Potsdam (AIP), Max-Planck-Institut für Astronomie (MPIA Heidelberg), Max-Planck-Institut für Astrophysik (MPA Garching), Max-Planck-Institut für Extraterrestrische Physik (MPE), National Astronomical Observatories of China, New Mexico State University, New York University, University of Notre Dame, Observatório Nacional / MCTI, The Ohio State University, Pennsylvania State University, Shanghai Astronomical Observatory, United Kingdom Participation Group, Universidad Nacional Autónoma de México, University of Arizona, University of Colorado Boulder, University of Oxford, University of Portsmouth, University of Utah, University of Virginia, University of Washington, University of Wisconsin, Vanderbilt University, and Yale University.

REFERENCES

- Aguado D. S., et al., 2019, *ApJS*, **240**, 23
- Albers S. M., et al., 2019, *MNRAS*, **490**, 5538
- Aloisi A., et al., 2007, *ApJ*, **667**, L151
- Annibali F., et al., 2013, *AJ*, **146**, 144
- Argudo-Fernández M., et al., 2015, *A&A*, **578**, A110
- Bertelli G., Bressan A., Chiosi C., Fagotto F., Nasi E., 1994, *A&AS*, **106**, 275
- Blanton M. R., Roweis S., 2007, *AJ*, **133**, 734
- Blanton M. R., et al., 2005, *AJ*, **129**, 2562
- Blanton M. R., et al., 2017, *AJ*, **154**, 28
- Boquien M., Burgarella D., Roehly Y., Buat V., Ciesla L., Corre D., Inoue A. K., Salas H., 2019, *A&A*, **622**, A103
- Bruzual G., Charlot S., 2003, *MNRAS*, **344**, 1000
- Bundy K., et al., 2015, *ApJ*, **798**, 7
- Calzetti D., Armus L., Bohlin R. C., Kinney A. L., Koornneef J., Storchi-Bergmann T., 2000, *ApJ*, **533**, 682
- Cappellari M., 2017, *MNRAS*, **466**, 798
- Cappellari M., Emsellem E., 2004, *PASP*, **116**, 138
- Cenarro A. J., Cardiel N., Gorgas J., Peletier R. F., Vazdekis A., Prada F., 2001, *MNRAS*, **326**, 959
- Chabrier G., 2003, *PASP*, **115**, 763
- Charlot S., Fall S. M., 2000, *ApJ*, **539**, 718
- Chevallard J., Charlot S., 2016, *MNRAS*, **462**, 1415
- Cid Fernandes R., Mateus A., Sodré L., Stasińska G., Gomes J. M., 2005, *MNRAS*, **358**, 363
- Conroy C., van Dokkum P., 2012, *ApJ*, **747**, 69
- Cushing M. C., Rayner J. T., Vacca W. D., 2005, *ApJ*, **623**, 1115
- Digby R., et al., 2019, *MNRAS*, **485**, 5423
- Dolphin A. E., Weisz D. R., Skillman E. D., Holtzman J. A., 2005, arXiv Astrophysics e-prints,
- Drory N., et al., 2015, *AJ*, **149**, 77
- Dye S., et al., 2006, *MNRAS*, **372**, 1227
- Feroz F., Hobson M. P., Bridges M., 2009, *MNRAS*, **398**, 1601
- Feroz F., Hobson M. P., Cameron E., Pettitt A. N., 2013, preprint, ([arXiv:1306.2144](https://arxiv.org/abs/1306.2144))
- Garrison-Kimmel S., et al., 2019, arXiv e-prints,
- Ge J., Mao S., Lu Y., Cappellari M., Yan R., 2019, *MNRAS*, **485**, 1675
- Girardi L., Bressan A., Bertelli G., Chiosi C., 2000, *A&AS*, **141**, 371
- Gunn J. E., et al., 2006, *AJ*, **131**, 2332
- Hambly N. C., et al., 2008, *MNRAS*, **384**, 637
- Heavens A., Panter B., Jimenez R., Dunlop J., 2004, *Nature*, **428**, 625
- Hewett P. C., Warren S. J., Leggett S. K., Hodgkin S. T., 2006, *MNRAS*, **367**, 454
- Janowiecki S., Salzer J. J., van Zee L., Rosenberg J. L., Skillman E., 2017, *ApJ*, **836**, 128
- Kauffmann G., 2014, *MNRAS*, **441**, 2717
- Kauffmann G., et al., 2003, *MNRAS*, **341**, 54
- Lan T.-W., Ménard B., Mo H., 2016, *MNRAS*, **459**, 3998
- Law D. R., et al., 2015, *AJ*, **150**, 19
- Law D. R., et al., 2016, *AJ*, **152**, 83
- Lawrence A., et al., 2007, *MNRAS*, **379**, 1599
- Le Borgne J.-F., et al., 2003, *A&A*, **402**, 433
- Li H., et al., 2018, *MNRAS*, **476**, 1765
- Lim S. H., Mo H. J., Lan T. W., Ménard B., 2017, *MNRAS*, **464**, 3256
- Lu Y., et al., 2014, *ApJ*, **795**, 123
- Lu Z., Mo H. J., Lu Y., Katz N., Weinberg M. D., van den Bosch F. C., Yang X., 2015, *MNRAS*, **450**, 1604
- Maraston C., 2005, *MNRAS*, **362**, 799
- Maraston C., Strömberg G., 2011, *MNRAS*, **418**, 2785
- Mateo M. L., 1998, *ARA&A*, **36**, 435
- Mo H. J., Mao S., 2004, *MNRAS*, **353**, 829
- Noll S., Burgarella D., Giovannoli E., Buat V., Marcellac D., Muñoz-Mateos J. C., 2009, *A&A*, **507**, 1793
- Peng Y.-j., Lilly S. J., Renzini A., Carollo M., 2012, *ApJ*, **757**, 4
- Rayner J. T., Cushing M. C., Vacca W. D., 2009, *ApJS*, **185**, 289
- Sacchi E., et al., 2016, *ApJ*, **830**, 3
- Sánchez-Blázquez P., et al., 2006, *MNRAS*, **371**, 703
- Smee S. A., et al., 2013, *AJ*, **146**, 32
- Telles E., Melnick J., 2018, *A&A*, **615**, A55
- Tolstoy E., Hill V., Tosi M., 2009, *ARA&A*, **47**, 371
- Valdes F., Gupta R., Rose J. A., Singh H. P., Bell D. J., 2004, *ApJS*, **152**, 251
- Vazdekis A., Sánchez-Blázquez P., Falcón-Barroso J., Cenarro A. J., Beasley M. A., Cardiel N., Gorgas J., Peletier R. F., 2010, *MNRAS*, **404**, 1639
- Vazdekis A., Koleva M., Ricciardelli E., Röck B., Falcón-Barroso J., 2016, *MNRAS*, **463**, 3409
- Wake D. A., et al., 2017, *AJ*, **154**, 86
- Weisz D. R., et al., 2011, *ApJ*, **739**, 5
- Weisz D. R., Dolphin A. E., Skillman E. D., Holtzman J., Gilbert K. M., Dalcanton J. J., Williams B. F., 2014, *ApJ*, **789**, 147
- Westera P., Lejeune T., Buser R., Cuisinier F., Bruzual G., 2002, *A&A*, **381**, 524
- Westfall K. B., et al., 2019, arXiv e-prints,
- Wright A. C., Brooks A. M., Weisz D. R., Christensen C. R., 2019, *MNRAS*, **482**, 1176
- Yan R., et al., 2016a, *AJ*, **151**, 8
- Yan R., et al., 2016b, *AJ*, **152**, 197
- Yang X., Mo H. J., van den Bosch F. C., Pasquali A., Li C., Barden M., 2007, *ApJ*, **671**, 153
- Zhao D. H., Jing Y. P., Mo H. J., Börner G., 2003, *ApJ*, **597**, L9
- Zheng Z., et al., 2019, arXiv e-prints,
- Zhou S., et al., 2019, *MNRAS*, **485**, 5256
- van den Bosch F. C., Aquino D., Yang X., Mo H. J., Pasquali A., McIntosh D. H., Weinmann S. M., Kang X., 2008, *MNRAS*, **387**, 79
- van der Wel A., et al., 2011, *ApJ*, **742**, 111

This paper has been typeset from a \LaTeX file prepared by the author.

APPENDIX A: POSTERIOR PREDICTIVE DISTRIBUTION OF THE $(G - K)$ COLOUR

In Bayesian context, once the posterior distribution $P(\theta|D, H)$ is obtained through a chosen posterior sampler, one can make predictions by marginalizing the desired likelihood function over the posterior distribution. For example, the posterior predictive distribution (PPD) of a set of observable quantities D' , given the constraining data D , can be written as

$$P(D'|D, H) = \int P(D'|\theta, H)P(\theta|D, H)d\theta \quad (\text{A1})$$

where $P(D'|\theta, H)$ is the desired likelihood function describing the probability distribution of D' expected from the model H specified by the parameter set θ . Note that the set of the predicted observable, D' , is not necessarily related to the constraining data D : D' can be anything that can be predicted by the model through $P(D'|\theta, H)$. For a complex model H , such as the one we are concerned here, the PPD cannot be obtained analytically. In this case, one can select a large sample of models, $\{\theta_l\} (l = 1, 2, \dots, L)$ (with L the sample size), from the posterior distribution, make a prediction for D' using each of the $\theta \in \{\theta_l\}$, and obtain a sample of the PPD, $P(D'|D, H)$, from the sample of D' obtained from $\{\theta_l\}$. The PPD so obtained can then be compared with the observational data of D' to check whether the original model can accommodate the observational data.

Once the PPD is obtained, one can check a specific model family using a procedure called the posterior predictive check (PPC). The basic idea is the following: if the model is correct then the data replicated from the model should have a distribution that can accommodate the observational data of D' , which will be denoted as \mathcal{D}' . Any significant discrepancy between the PPD and \mathcal{D}' will signify the inadequacy of the hypothesis H . To compare the PPD with the data, one can define a test statistic $T(D')$. The tail probability (the p -value) of the test statistic can then be used to assess the ‘goodness of fit’ of the model to the data. In the Bayesian context, the

p-value can be defined as

$$\begin{aligned} p &= P[T(D') \geq T(\mathcal{D}'|D)] \\ &= \int \int I_{T(D') \geq T(\mathcal{D}')} P(D'|\theta, H) P(\theta|D, H) d\theta dD', \quad (\text{A2}) \end{aligned}$$

where I_q is the indication function for the condition q ($I_q = 1$ if q is true and 0 otherwise). If the observational data \mathcal{D}' is incompatible with the model, then the test statistic from the data, $T(\mathcal{D}')$, should be a significant outlier of the distribution of $T(D')$ predicted by the model. In practice, if the posterior predictive p-value is close to 0 or 1, then the model is most likely inadequate.

Here we use the models constrained by the MaNGA data to make predictions for the NIR photometry and check whether or not the models can also accommodate the NIR data. We use the fitting of galaxy 9490-6104 as an example. To get the PPD, we draw $L = 1000$ samples from the posterior distribution obtained from the MaNGA spectra of this galaxy using the Γ model and $\Gamma+B$ model, respectively. We then use the $(g-K)$ colour as the predicted observable D' . The PPDs derived from the two SFH models are shown in Fig. A1. The PPD of the Γ model peaks at $(g-K) = 2.61$ while that of the $\Gamma+B$ model at $(g-K) = 2.56$. The measurement from WSA for this galaxy is $(g-K) = 2.39$. These results indicate that even with the inclusion of an early burst population, the lack of constraints from NIR bands may still lead to some bias in the stellar population.

As we have chosen the $(g-K)$ colour (denoted as K' for convenience) as our test observable, we can use a χ^2 -like test statistic to perform the PPC on the fitting results. The corresponding test statistic can be written as

$$T_l(K'_l) = \frac{(K'_l - \bar{K}')^2}{\sigma'^2} \quad (\text{A3})$$

where \bar{K}' and σ' are, respectively, the mean and standard deviation of the PPD obtained from a posterior sample. For an observed $(g-K)$ colour, K'_o , the corresponding statistic is

$$T_o = \frac{(K'_o - \bar{K}')^2}{\sigma'^2}. \quad (\text{A4})$$

The p -value defined by equation (A2) can then be obtained. Fig. A2 shows the distribution of the test statistics T and the T_o obtained from the observed $(g-K)$ colour, together with the p -value obtained from equation (A2). The p -value is 0.0 in both of the two fitting results, indicating that the models are over-constrained by the MaNGA spectra.

As a comparison, we can make inferences by including the observed $(g-K)$ colour as a constraint. Using the likelihood function in equation (4), we apply the posterior predictive check method to the fitting results. The results are shown in the bottom panels of Fig. A1 and Fig. A2, respectively. By including this additional constraint, the $\Gamma+B$ model can now pass the PPC test, while the Γ model still fail to reproduce the observation.

To statistically characterize the results, we apply PPC to all the 19 galaxies that have UKIDSS NIR measurements. We derive the PPD from the posterior distributions of the fitting results and calculate the 3σ level of the distribution as an approximate boundary. Successful models should predict a PPD that covers the probable observational ranges, and so the observation data are expected to fall within the boundary. We plot the difference between the predicted and observational $(g-K)$ colours, denoted as Δ_{g-K} , in Fig. A3, and show the corresponding 3σ boundary as error bars. As one can see, if only the MaNGA spectra are used in the fitting, both the SFH models fail to pass the PPC test in many case. In contrast, if the NIR data is included in the fitting, the $\Gamma+B$ model can generally pass this test, while the Γ still fails to reproduce the observation in many cases (see blue points in Fig. A3). These results strengthen our conclusion that the $\Gamma+B$ model is a better description of the true SFH. They also indicate the importance of using the NIR data in order to correctly model the stellar population.

However, those results also signify tensions between the predictions based on high-resolution spectra with limited wavelength coverage and those based on broadband photometry covering a larger wavelength range. Ideally, if the optical spectra do not provide tight constraints on the stellar populations that can affect the NIR fluxes significantly, the posterior distribution inferred from the optical data should be broad enough to accommodate the observed NIR fluxes. In reality, however, the situation may be more complicated. Spectral synthesis modeling of observed spectra is high

dimensional, and the posterior distribution may be complex. If the model cannot describe the observed spectra perfectly, there is no guarantee that the 'best-fit' model derived from part of a spectrum is also the best-fit model for the entire spectrum. The posterior distribution inferred from part of the spectrum may then lead to biased predictions for the spectrum outside the observed window. In principle, any uncertainties in the model itself should be included in the likelihood function. Unfortunately, such uncertainties are difficult to quantify for the spectral synthesis model concerned here. In such a case, one should use all constraints available to obtain a set of model parameters that best describe all the data.

Uncertainties of the SSP templates are perhaps the most important in affecting the spectral synthesis model. Available Models based on different SSP templates, with their own merits and shortcomings, may work better in some cases but worse in others. To test this, we use our fitting results based on the BC03 model and the mixture model described in §5.2. The Δ_{g-K} predicted by these two models are shown in Fig. A4 in comparison with those predicted by the E-MILES model. As we can see, the BC03 model can reach consistencies between the optical fitting and the NIR observations in some cases where E-MILES fails, and vice versa.

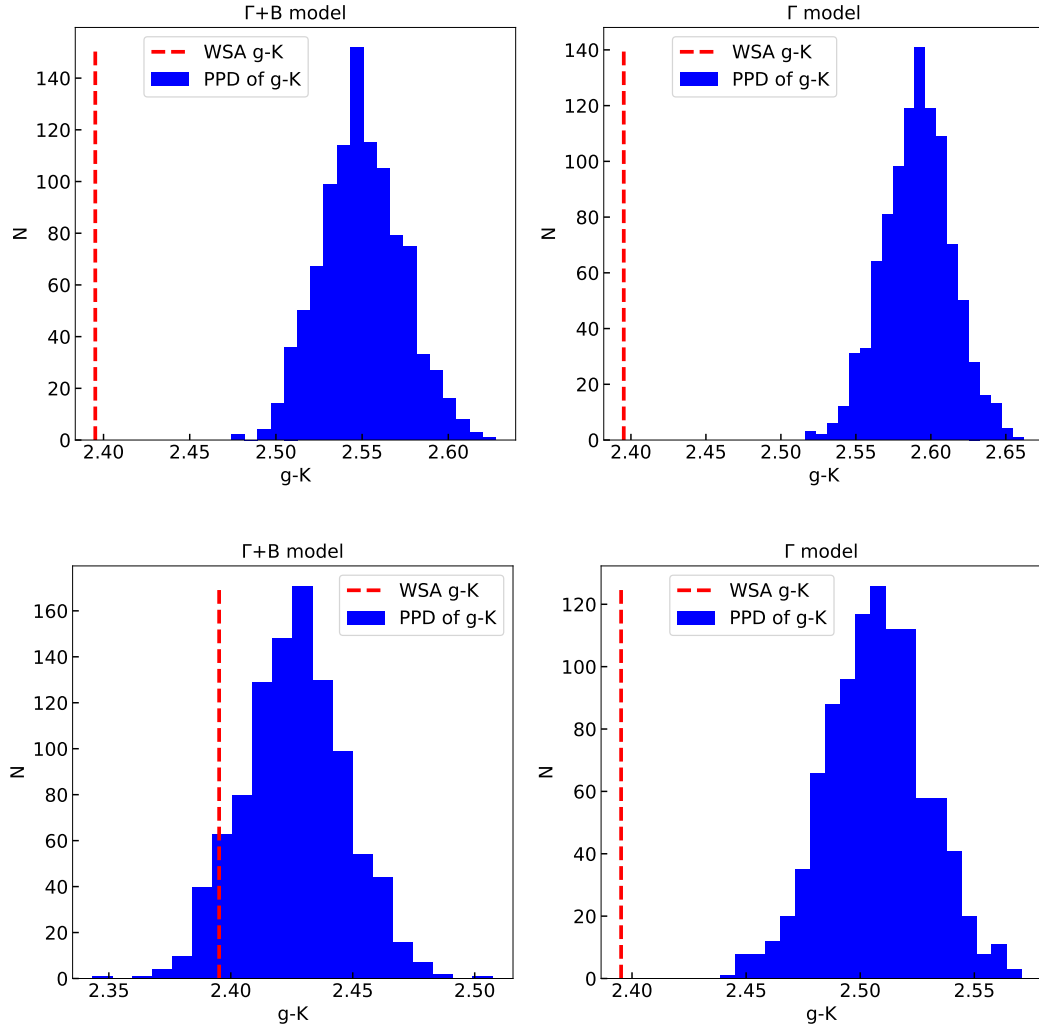


Figure A1. Histograms showing the posterior predictive distribution of the $(g-K)$ colour. Left panels are results obtained using the $\Gamma+B$ model, while right panels are using the Γ model. Top panels are based on MaNGA optical spectra, while bottom panels are results that include the $(g-K)$ colour. Red dash line in each panel denotes the $(g-K)$ colour from UKIDSS.

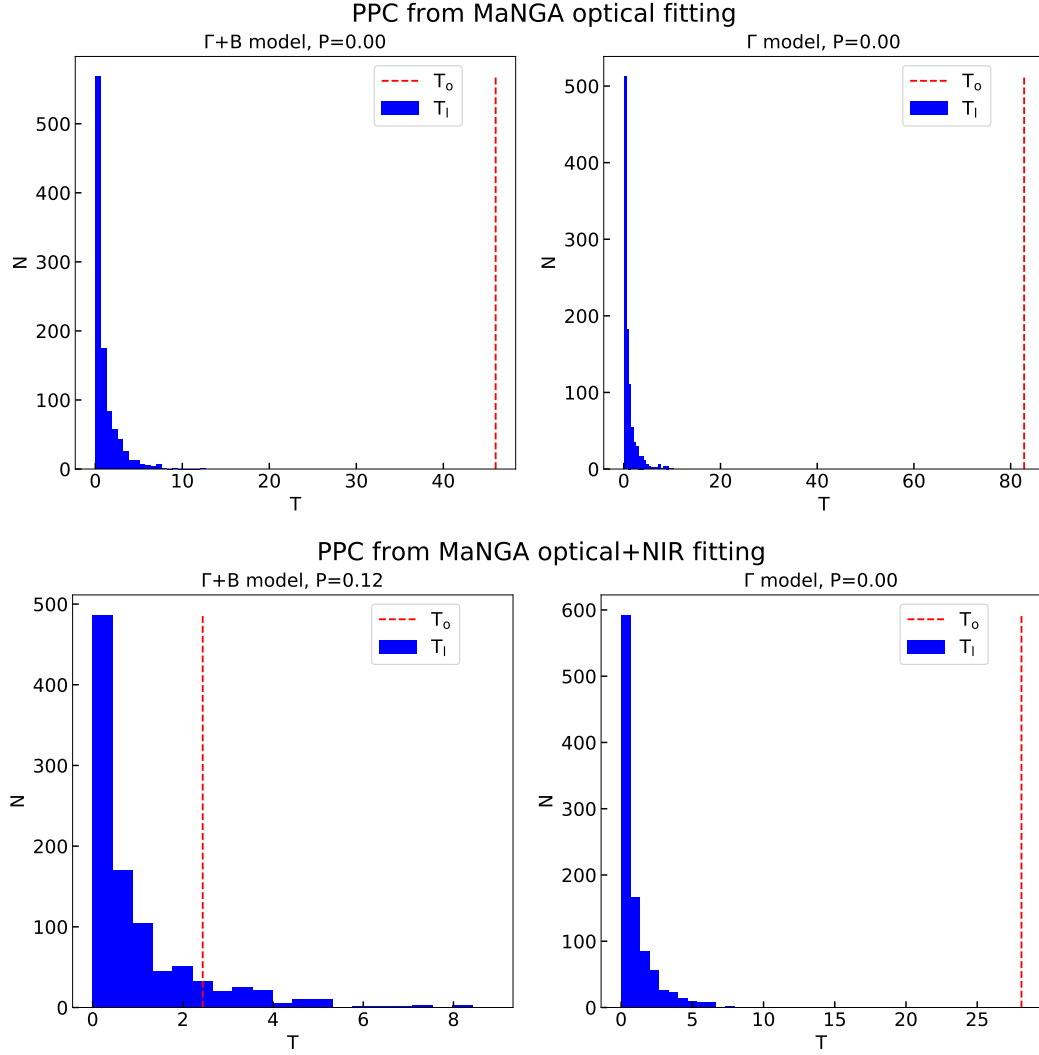


Figure A2. Posterior predictive check for the Γ +B model (left) and the Γ model (right). Histograms show the distribution of the test statistics T_I for the 1000 samples drawn from the posterior distribution. Top panels are results based on fitting the MaNGA optical spectra, while bottom panels are results that include the $(g - K)$ colour. Red dash line in each panel denotes the test statistics T_O calculated from the UKIDSS observation.

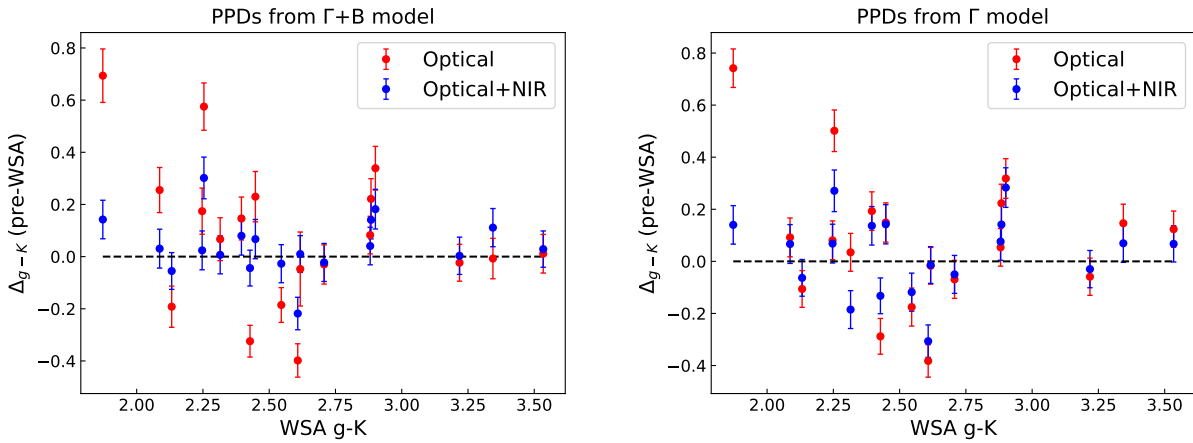


Figure A3. Differences between the posterior predicted $(g - K)$ colour from fitting MaNGA optical spectra and the WSA values. Results are derived from Γ +B model (left) and Γ model (right), red and blue dots are from MaNGA optical fitting and optical+NIR fitting, respectively. Error bars denote the 3σ level of the PPD.

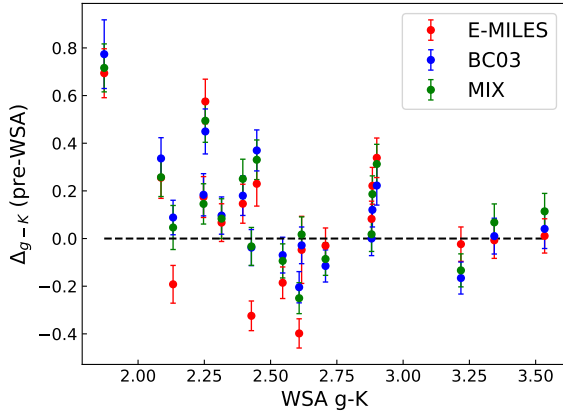


Figure A4. Differences between the posterior predicted ($g-K$) colour from fitting MaNGA optical spectra and the WSA values. Results are derived from E-MILES (red), BC03 (blue), and mixed models (green). Error bars are the 3σ level of the PPD.